

Deep material networks for fiber suspensions with infinite material contrast

Benedikt Sterr¹, Sebastian Gajek¹, Andrew Hrymak², Matti Schneider³, and Thomas Böhlke¹

¹Karlsruhe Institute of Technology (KIT), Institute of Engineering Mechanics

²University of Western Ontario, Department of Chemical and Biochemical Engineering

³University of Duisburg-Essen, Institute of Engineering Mathematics

correspondence to: thomas.boehlke@kit.edu

June 18, 2024

Abstract

We extend the laminate based framework of direct Deep Material Networks (DMNs) to treat suspensions of rigid fibers in a non-Newtonian solvent. To do so, we derive two-phase homogenization blocks that are capable of treating incompressible fluid phases and infinite material contrast. In particular, we leverage existing results for linear elastic laminates to identify closed form expressions for the linear homogenization functions of two-phase layered emulsions. To treat infinite material contrast, we rely on the repeated layering of two-phase layered emulsions in the form of coated layered materials. We derive necessary and sufficient conditions which ensure that the effective properties of coated layered materials with incompressible phases are non-singular, even if one of the phases is rigid.

With the derived homogenization blocks and non-singularity conditions at hand, we present a novel DMN architecture, which we name the Flexible DMN (FDMN) architecture. We build and train FDMNs to predict the effective stress response of shear-thinning fiber suspensions with a Cross-type matrix material. For 31 fiber orientation states, six load cases, and over a wide range of shear rates relevant to engineering processes, the FDMNs achieve validation errors below 4.31% when compared to direct numerical simulations with Fast-Fourier-Transform based computational techniques. Compared to a conventional machine learning approach introduced previously by the consortium of authors, FDMNs offer better accuracy at an increased computational cost for the considered material and flow scenarios.

Keywords: Deep Material Network; Fiber-reinforced composites; Non-Newtonian suspension; Infinite material contrast; Supervised machine learning; Effective viscosity

1 Introduction

1.1 State of the art

Especially because of their high specific stiffness, fiber reinforced composites are widely used for lightweight design, particularly in the transport and energy sectors [1,2]. During the design process of fiber reinforced composite components, combinations of molding simulations and structural simulations are central to facilitate use case appropriate and material oriented design through digital twins [3] and virtual process

chains [4–6]. In molding simulations of fiber reinforced composite parts, accurate prediction of the local fiber suspension viscosity is vital to correctly estimate process parameters [7, 8] and other engineering quantities. In particular, the fiber orientation and the fiber volume distributions [9], the flow fields, [10], as well as the final part properties [10–12] depend on the suspension viscosity. However, in component scale simulations, it is computationally infeasible to fully resolve the microstructure of the whole domain of interest to compute the suspension viscosity. For this purpose, analytical and computational homogenization methods are valuable tools to provide viscosity estimates for molding simulations. However, significant challenges arise for the holistic analytical modelling of the suspension viscosity, because the suspension viscosity depends on the local microstructure [13], the fiber volume fraction [14], and the fiber orientation state [15]. Additionally, the flow field [16, 17] and the melt temperature [18] influence the suspension viscosity as well. Furthermore, typical matrix materials in fiber suspensions show non-Newtonian behavior, which adds additional complexity to the derivation of appropriate models for the suspension viscosity.

Depending on the fiber concentration of the suspension and the behavior of the matrix material, different homogenization approaches have been proposed. According to Pipes et al. [19, §1] the fiber concentration regimes may be defined using the fiber volume fraction c_F and the fiber aspect ratio r_a as follows. The dilute regime is defined through $c_F < (1/r_a)^2$, the semi-dilute regime through $(1/r_a)^2 < c_F < 1/r_a$, the concentrated regime through $1/r_a < c_F$, and the hyperconcentrated regime through $r_a > 100$ [19]. Goddard [20, 21], and Souloumiac and Vincent [22] proposed self-consistent analytical models for different concentration regimes. The models by Goddard are restricted to the dilute and semi-dilute regimes, while the models by Souloumiac and Vincent are applicable to the dilute, semi-dilute, and concentrated regimes. Both models agree well with experimental results [23] qualitatively. However, the quantitative prediction accuracy could be improved and varies strongly depending on the shear rate and fiber volume fraction. Similarly, a semi-analytical model proposed by Férec et al. [24] for Ellis and Carreau-type matrix behavior replicates the steady state flow solution of a simple shear flow, but its accuracy varies with the shear rate and the fiber volume fraction. By incorporating uniformly distributed fiber misalignments with an orientation averaging approach [25, 26], Pipes et al. [19, 27–29] derived models for the concentrated and hyper-concentrated regime. The models are only applicable to collimated fiber arrays, but their predictions agree well with experimental studies by Binding [30]. Combining orientation averaging with a deformation mode and microstructure dependent informed isotropic viscosity, Favaloro et al. [31] derived a model that aims to improve available molding simulation solvers with only small modifications. Depending on the deformation mode and the approximated anisotropic viscosity, the prediction quality of the model varies. However, molding simulations using the model successfully predicted the shell-core effect that is common in a wide variety of fiber molding applications [9, 11]. Overall, predicting the suspension viscosity accurately over the wide variety of processing conditions used for engineering systems proves difficult, which includes recent developments [32, 33].

The development of homogenization methods is accompanied by considerable difficulties in studying the fiber suspension viscosity experimentally. In rheometer studies, certain transient effects like fiber breakage and fiber reorientation are difficult to quantify during the experiment. Thus, it is hard to link a specific fiber orientation state and a specific fiber length distribution to a measured viscosity [30, 34]. Furthermore, the measurement results may be affected by the interaction between the fibers and the measurement devices [35].

In view of these difficulties, computational techniques offer an extraordinary approach to study the effective viscosity of fiber suspensions with non-Newtonian solvents by resolving the local fields of interest and providing insights, which are hard to obtain otherwise. Combining a mass tracking algorithm for the free surface representation, a lattice Boltzmann method for fluid flow, and an immersed boundary

procedure for the interaction between fluid and rigid particles, Švec et al. [36] studied slump tests of rigid fibers and rigid spherical particles suspended in a Bingham-type fluid. They compared slump tests of the suspension with a slump test of the pure matrix material, and observed a smaller spread and an increased height in the test of the suspension material, which implies an increased effective yield stress in the suspension. Domurath et al. [37] employed a Finite Element Method (FEM) based approach to study the transversely isotropic fluid equation by Ericksen [25]. They investigated the rheological coefficients and found that the model by Souloumiac and Vincent [22] overpredicts the orientation dependence of a rheological coefficient. Extending work by Bertóti et al. [38] on suspensions with Newtonian solvents, Sterr et al. [17] used Fast Fourier Transform (FFT) based computational techniques [39] and the RVE method [40] to study the effective viscosity of fiber suspensions with non-Newtonian solvents. They investigated the effects of anisotropic shear-thinning on the effective suspension viscosity for varying fiber volume fractions, shear rates, and flow scenarios.

Accurate computational predictions of the microscopic behavior of a composite often require significant computational effort [41–45], which motivates the use of fast data based surrogate models for component scale simulations [46]. Ashwin et al. [47, 48] trained a Multi-Layer-Perceptron, a Convolutional Neural Network, and a U-Net [49] on particle resolved simulation data to predict fluid forces in dense ellipsoidal particle suspensions. They restricted to Newtonian matrix behavior and trained the networks on data for various Reynolds numbers and fiber volume fractions. Depending on the considered combination of Reynolds number and particle volume fraction, the prediction accuracy of the surrogate models varies. Boodaghizaji et al. [50] use a multi-fidelity approach with neural networks and Gaussian processes to predict the steady state viscosity of fiber suspensions with a Newtonian solvent. To form the training data set, they combine low-fidelity estimates from constitutive equations with high-fidelity data obtained from numerically solving the involved partial differential equation system. The prediction accuracy of the multi-fidelity neural network and the multi-fidelity Gaussian process for simple shear flow depends strongly on the investigated parameters, especially the fiber volume fraction. Sterr et al. [51] derived four models for fiber suspensions with a Cross-type matrix fluid by combining FFT-based computational homogenization techniques with supervised machine learning. They investigated the anisotropic shear-thinning characteristics of the suspension viscosity for a variety of fiber orientation states via computational experiments, and formulated model candidates based on the observed phenomena. Using supervised machine learning techniques, they identified the model parameters from computational data, so that three of the four models were able to predict the fiber suspension viscosities to engineering accuracy for a wide range of engineering load cases. Generally, in addition to accurate estimation, extrapolation beyond the training data, as well as ensuring thermodynamical consistency prove challenging in the construction of surrogate models.

In the context of solid materials without kinematic constraints, Liu et al. [52, 53] proposed Deep Material Networks (DMNs) as surrogate models for the full-field computational homogenization of microstructured materials. Their approach is based on nesting rotated laminates in an N -ary tree structure of N -phase laminates, and thus constructing a micromechanically motivated deep learning architecture. The volume fractions and rotations of the DMN are then identified via supervised machine learning on linear elastic data. Remarkably, even if a DMN is trained on data obtained by solving linear homogenization problems, the predictions of the DMN for non-linear homogenization problems are impressively accurate. Gajek et al. [54] further developed the DMN architecture into the rotation free direct DMN architecture. Direct DMNs feature a faster and more robust training process, as well as an efficient evaluation scheme for non-linear problems. Gajek et al. [54] also showed that the thermodynamic consistency of the laminates is preserved in (direct) DMNs, such that the resulting DMN is thermodynamically consistent as well. Furthermore, Gajek et al. [54] proved that non-linear homogenization is determined by linear

homogenization to first order for two-phase materials. In a later article, Gajek et al. [46] used direct DMNs to accelerate two-scale FE simulations of fiber reinforced composites by augmenting direct DMNs with the fiber orientation interpolation concept introduced by Köbler et al. [55]. Alternatively, DMN parameters may be interpolated with regard to microstructural parameters by a posteriori interpolation as proposed by Liu et al. [56] and Huang et al. [57], or by augmenting DMNs with neural networks as proposed by Li [58]. To leverage the capabilities of direct DMNs in concurrent thermomechanical two-scale simulations of composite components, Gajek et al. [59] further extended the direct DMN architecture to incorporate thermomechanical coupling. Also in a thermomechanical setting, Shin et al. [60] trained DMNs on linear thermoelastic data instead of linear elastic data, which improved the quality of fit for the effective thermal expansion properties, but only slightly affected the non-linear prediction quality of the DMNs. Additionally, they employed DMNs for uncertainty quantification, and for the inverse problem of optimizing a thermal boundary condition to achieve a desired thermo-elasto-viscoplastic response. By developing an inelastically-informed training strategy for DMNs, Dey et al. [61] successfully predicted the creep behavior of fiber reinforced thermoplastics, which involves multiple scales in both space and time. This enabled the inverse calibration of parameters for creep and plasticity constitutive equations by using DMNs as surrogates for otherwise costly FFT-based computations [62]. Furthermore, Dey et al. [63] leveraged DMNs in combination with fiber orientation interpolation [55] to characterize the behavior of fiber reinforced thermoplastics including damage, plasticity, and creep. Overall, DMNs were extended and applied to treat a wide variety of problems, such as interface damage [64], the modeling of multiscale strain localization [65], problems involving woven materials [66] and porous materials [67], as well as the architecture independent treatment of multi-phase composites [68].

For composites with kinematically unconstrained solid phases, the presented literature provides compelling evidence for the accuracy and versatility of (direct) DMNs. However, the (direct) DMN architecture has yet to be applied to composites involving fluids or infinite material contrast, which is required for suspensions of rigid fibers. Because (direct) DMNs are based on laminates of solids, the treatment of fluids with a DMN architecture requires a different type of building block. Additionally, treatment of infinite material contrast with DMNs is challenging, because the rank-one laminates of a DMN have singular effective properties if one of the phases is singular, i.e., rigid. Therefore, the singular effective properties of the rank-one laminates may propagate through the whole DMN during the training and evaluation processes, rendering the effective properties of the DMN singular as well. In this article we address these issues and propose an architecture to treat suspensions of rigid fibers.

1.2 Contributions

In this work, we extend the direct DMN architecture for kinematically unconstrained solid phases with finite material contrast to an architecture that is able to treat suspensions of rigid fibers. In particular, this task requires the treatment of fluid phases and infinite material contrast. We name this architecture the Flexible DMN (FDMN) architecture. To treat fluid materials with FDMNs, we derive homogenization blocks for layered emulsions that are governed by Stokes flow, and consist of possibly incompressible phases with finite material contrast. In section 2.1, we establish that the velocity field in this type of layered material is phase-wise affine, if the dissipation potentials of the phases are strictly rank-one convex. We use this result and follow an analytical procedure described by Milton [69, §9] to derive the closed form linear homogenization function of the considered layered emulsions in section 2.2. To treat infinite material contrast, we study a particular type of layered material, namely, coated layered materials (CLMs), in section 2.3. We obtain closed form homogenization functions for CLMs with kinematically unconstrained or incompressible phases. With the objective of using CLMs as FDMN building blocks

in the presence of rigid fibers, we derive conditions for the required number of layering directions and their orientation, such that the effective properties of CLM are non-singular. We do so for CLMs with incompressible and rigid phases.

In section 3, we present the FDMN architecture as an extension of the (direct) DMN architecture. An FDMN arises by replacing the rank-one laminates of a (direct) DMN with rank-one layered materials capable of treating fluids, and non-singular CLMs capable of treating infinite material contrast. Also, we discuss the material sampling, the offline training procedure, as well as the online evaluation of FDMNs in the context of incompressible rigid fiber suspensions. We apply FDMNs to predict the viscous response of fiber polymer suspensions in section 4, demonstrating both the ability to handle incompressible fluid phases and infinite material contrast. We use FFT-based computational homogenization techniques to generate linear training data and non-linear validation data for shear-thinning fiber suspensions with a Cross-type matrix behavior, and a fiber volume fraction of 25%. We consider 31 different fiber orientation states and a variety of incompressible elongational and shear flows. Using the computational data, we train FDMNs for all fiber orientation states, and study the prediction accuracy of the FDMNs in the non-linear case. For all investigated load cases and microstructures, the FDMNs achieve validation errors below 4.31% over a wide range of shear rates relevant to engineering processes. Not considering the time required to generate the training data and to train an FDMN, the FDMNs achieve speedup factors between 11785 and 17225 compared to FFT-based computations. Finally, we compare the prediction accuracy of the FDMN based approach with a different machine learning approach by Sterr et al. [51], and find that FDMNs offer better accuracy and flexibility at a higher computational cost for the considered material and flow scenarios.

2 Homogenization of layered emulsions with infinite material contrast

2.1 Phase-wise affine displacement and velocity fields in laminates and emulsions

Like for (direct) DMNs, the building blocks of an FDMN should admit linear homogenization functions in closed form, and there should exist efficient solution schemes to compute the stress response of the building blocks in case their phases are non-linear. In analogy to the laminate based architecture of the (direct) DMN, we thus consider layered emulsions as the building blocks of the FDMN architecture. Like laminates, layered emulsions consist of multiple, possibly non-linear, fluid materials, that are arranged such that every phase boundary between the phases is orthogonal to the layering direction $\mathbf{n} \in \mathcal{S}^2$, on the 2-sphere \mathcal{S}^2 . For the offline training and the online evaluation of an FDMN with layered emulsions as building blocks, knowing the homogenization functions of layered emulsions with linear and non-linear phases is necessary. Primarily, we look for similarities between the homogenization of layered emulsions and solid laminates that can be leveraged. In laminates, the displacement fields are phase-wise affine, and we wish to know if the velocity fields in layered emulsions belong to a particular class of fields as well. If the velocity fields are phase-wise affine, established solution techniques on (direct) DMN architectures [54] can be employed for the online evaluation of the FDMN, and convenient linear homogenization equations can be employed for the offline training. We follow a procedure detailed by Kabel et al. [70] on the homogenization of laminates, and establish the existence and uniqueness of phase-wise affine velocity fields in a particular type of emulsion. We consider a K -phase layered emulsion with layering direction \mathbf{n} , which, similar to a laminate, is constructed by arranging K -phases so that the direction \mathbf{n} is orthogonal

to all phase boundaries. The emulsion occupies a rectangular and periodic volume $Y \subset \mathbb{R}^3$, and consists of non-Newtonian phases with rank-one convex dissipation potential densities $\Psi_k : (\mathbb{R}^3)^{\otimes 2} \rightarrow \mathbb{R}$, such that

$$\Psi_k(\mathbf{L} + \beta \mathbf{a} \otimes \mathbf{b}) \leq \beta \Psi_k(\mathbf{L} + \mathbf{a} \otimes \mathbf{b}) + (1 - \beta) \Psi_k(\mathbf{L}) \quad \forall \beta \in [0, 1], \mathbf{a}, \mathbf{b} \in \mathbb{R}^3 \setminus \{\mathbf{0}\}, \quad (2.1)$$

where $\mathbf{L} \in (\mathbb{R}^3)^{\otimes 2}$ denotes the velocity gradient, and the operator $(\cdot)^{\otimes a}$ constructs a tensor space of a -th order. Also, $Y_k \subset Y$ denotes the sub volume of the k -th phase, and the phases do not intersect, i.e.,

$$Y_j \cap Y_k = \emptyset \quad \text{if } j \neq k, \quad (2.2)$$

and form the volume Y , such that

$$Y = \bigcup_{j=1}^K Y_j. \quad (2.3)$$

Let the operator $\langle \cdot \rangle_Y$ denote volume averaging of a quantity over a volume Y , i.e.,

$$\langle \cdot \rangle_Y \equiv \frac{1}{|Y|} \int_Y (\cdot) dY(\mathbf{x}) \quad \text{with} \quad |Y| \equiv \int_Y dY(\mathbf{x}). \quad (2.4)$$

Then, we express the velocity field $\mathbf{v} : Y \rightarrow \mathbb{R}^3$ as

$$\mathbf{v} = \bar{\mathbf{L}}\mathbf{x} + \hat{\mathbf{v}}, \quad \text{with} \quad \langle \nabla \hat{\mathbf{v}} \rangle_Y = \mathbf{0}, \quad (2.5)$$

where $\bar{\mathbf{L}} \in (\mathbb{R}^3)^{\otimes 2}$ stands for the prescribed effective velocity gradient and $\hat{\mathbf{v}}$ is the velocity fluctuation field. Accordingly, the periodic dissipation potential density function $\Psi : Y \times (\mathbb{R}^3)^{\otimes 2} \rightarrow \mathbb{R}$ of the emulsion is defined through

$$\Psi(\mathbf{x}, \nabla^s \mathbf{v}) = \sum_i^K \chi_k(\mathbf{x}) \Psi_k(\mathbf{x}, \nabla^s \mathbf{v}), \quad (2.6)$$

where $\chi_k : Y \rightarrow \{0, 1\}$ refers to the characteristic function of the sub volume Y_k , and ∇^s stands for the symmetrized gradient. Let the flow inside the emulsion be governed by Stokes flow, i.e., the advectorial forces in the layered emulsion are small in contrast to the viscous forces, then the steady state balance of mass

$$\text{div}(\rho \mathbf{v}) = 0, \quad (2.7)$$

where $\rho : Y \rightarrow \mathbb{R}$ denotes the mass density field, is satisfied. Additionally, the stress field

$$\boldsymbol{\sigma} = \mathcal{S}(\cdot, \bar{\mathbf{D}} + \nabla^s \hat{\mathbf{v}}) \quad (2.8)$$

in terms of the effective strain rate tensor $\bar{\mathbf{D}} = (\bar{\mathbf{L}} + \bar{\mathbf{L}}^\top)/2$, and the associated stress operator \mathcal{S} on the space of symmetric second order tensors $\text{Sym}(3) \subset (\mathbb{R}^3)^{\otimes 2}$ [71]

$$\mathcal{S} : Y \times \text{Sym}(3) \rightarrow \text{Sym}(3), \quad (2.9)$$

$$(\mathbf{x}, \mathbf{D}) \mapsto \frac{\partial \Psi}{\partial \mathbf{D}}(\mathbf{x}, \mathbf{D}), \quad (2.10)$$

satisfies the balance of linear momentum without inertial effects and volume forces

$$\text{div} \boldsymbol{\sigma} = \mathbf{0}. \quad (2.11)$$

Therefore, the effective response of the emulsion is obtained from the minimization problem

$$\langle \Psi(\mathbf{x}, \bar{\mathbf{D}} + \nabla^s \hat{\mathbf{v}}) \rangle_Y \longrightarrow \min_{\hat{\mathbf{v}} \in \mathcal{A}} \quad (2.12)$$

where \mathcal{A} stands for the admissible set

$$\mathcal{A} = \{ \hat{\mathbf{v}} : Y \rightarrow \mathbb{R}^3 \mid \operatorname{div}(\rho \mathbf{v}) = 0 \quad \text{and} \quad \langle \nabla \hat{\mathbf{v}} \rangle_Y = \mathbf{0} \} \quad (2.13)$$

Hence, assuming there is no slip between the phases, the proof by Kabel et al. [70, §2] extends to layered emulsions with finite material contrast. Therefore, if the dissipation potential densities Ψ_k are strictly rank-one convex, there exists a unique minimizer $\hat{\mathbf{v}}$ in the class of phase-wise affine velocity fields. As a special case, this is also true for incompressible Stokes flows, for which the balance of mass simplifies to

$$\operatorname{div} \mathbf{v} = 0. \quad (2.14)$$

In the following, we use the term *layered emulsion* only for the type of emulsion defined above.

2.2 Two-phase layered emulsions with Newtonian phases

Similar to two-phase laminates of linear elastic solid materials, we wish to find a convenient closed form expression for the linear homogenization function of two-phase layered emulsions. With the goal of using layered emulsions as building blocks of an FDMN, we dedicate this section to deriving such a closed form expression for two-phase layered emulsions with kinematically unconstrained or incompressible Newtonian phases. For this purpose, we employ the results of the previous section 2.1, and extend an existing homogenization approach for two-phase laminates of linear elastic phases by Milton [69, §9]. To emphasize the link between the linear homogenization of laminates and layered emulsions we define the class of linear materials \mathcal{M} , and study layered materials of solids and fluids in parallel. A material m_k in the class of linear materials \mathcal{M} is characterized by the primal material tensor \mathbb{M}_k or its dual tensor $\mathbb{K}_k \equiv \mathbb{M}_k^{-1}$, such that

$$(\mathbb{M}_k, \mathbb{K}_k) \in \{(\mathbb{M}^+)^2, (\mathbb{M}_0^+)^2\}. \quad (2.15)$$

Here, the convex cones $\mathbb{M}^+ \subset (\mathbb{R}^3)^{\otimes 4}$ and $\mathbb{M}_0^+ \subset (\mathbb{R}^3)^{\otimes 4}$ comprise all fourth order tensors $\mathbf{X} \in (\mathbb{R}^3)^{\otimes 4}$, which are positive definite on the vector spaces of symmetric second order tensors $\operatorname{Sym}(3)$ and traceless symmetric second order tensors $\operatorname{Sym}_0(3) \subset \operatorname{Sym}(3)$, respectively. Additionally, a tensor $\mathbb{X} \in \{\mathbb{M}^+, \mathbb{M}_0^+\}$ has minor and major symmetries

$$\mathbb{X} = \mathbb{X}^{\text{T}_H} = \mathbb{X}^{\text{T}_L} = \mathbb{X}^{\text{T}_R}, \quad (2.16)$$

and a tensor $\mathbb{X} \in \mathbb{M}_0^+$ maps the second order unit tensor \mathbf{I} to zero, such that

$$\ker \mathbb{X} = \mathbf{I}, \quad \text{i.e.,} \quad \mathbb{X}[\mathbf{I}] = \mathbf{0}. \quad (2.17)$$

Here, we define the map $\mathbb{T}[\mathbf{Y}]$ in component form and in the standard basis of \mathbb{R}^3 as

$$\mathbb{T}[\mathbf{Y}] \hat{=} T_{ijkl} Y_{kl}, \quad \text{for some} \quad \mathbf{Y} \in (\mathbb{R}^3)^{\otimes 2}, \mathbb{T} \in (\mathbb{R}^3)^{\otimes 4}. \quad (2.18)$$

Any material $m_k \in \mathcal{M}$ follows the linear constitutive equations

$$\boldsymbol{\sigma}^{co} = \mathbb{M}_k[\nabla^s \mathbf{w}] \quad \text{and} \quad \nabla^s \mathbf{w} = \mathbb{K}_k[\boldsymbol{\sigma}^{co}], \quad (2.19)$$

if the material m_k is not subjected to kinematic constraints, or the constitutive equation

$$\boldsymbol{\sigma}^{ico} = \boldsymbol{\tau} - p\mathbf{I} = \mathbb{M}_k[\nabla^s \mathbf{w}] - p\mathbf{I}, \quad \text{and} \quad \nabla^s \mathbf{w} = \mathbb{K}_k[\boldsymbol{\tau}], \quad (2.20)$$

if the material m_k is incompressible. Here, \mathbf{w} denotes the field associated with the type of material m_k , i.e., the displacement field \mathbf{u} for linear elastic solids or the velocity field \mathbf{v} for linearly viscous fluids. For the constitutive equation (2.20) we use an additive split of the stress field $\boldsymbol{\sigma}$

$$\boldsymbol{\sigma} = \boldsymbol{\tau} - p\mathbf{I}, \quad (2.21)$$

into the deviatoric stress field $\boldsymbol{\tau} : Y \rightarrow \text{Sym}_0(3)$ and the pressure field $p : Y \rightarrow \mathbb{R}$. Here, we use $Y \subset \mathbb{R}^3$ to denote the volume occupied by a two-phase layered material, i.e., a laminate or a layered emulsion, and $Y_1, Y_2 \subset Y$ to denote the volume occupied by the two phases $m_1, m_2 \in \mathcal{M}$ of the layered material. We define the effective properties $(\bar{\mathbb{M}}, \bar{\mathbb{K}}) \in \{(M^+)^2, (M_0^+)^2\}$ of the layered material in the sense of the Hill-Mandel condition [72, 73]

$$\langle \boldsymbol{\sigma} \cdot \nabla^s \mathbf{w} \rangle_Y = \langle \boldsymbol{\sigma} \rangle_Y \cdot \langle \nabla^s \mathbf{w} \rangle_Y \equiv \bar{\mathbb{M}} \cdot (\langle \nabla^s \mathbf{w} \rangle_Y \otimes \langle \nabla^s \mathbf{w} \rangle_Y). \quad (2.22)$$

Then, for perfectly bonded laminates of linear solid materials without kinematic constraints, a closed form expression for the primal or dual effective properties of the laminate $\bar{\mathbb{A}} \in \{\bar{\mathbb{M}}, \bar{\mathbb{K}}\}$ can be derived using the procedure detailed by Milton [69, §9], such that

$$\left((\bar{\mathbb{A}} - \mathbb{A}_0)^{-1} + \Gamma_{\mathbb{A}_0}(\mathbf{n}) \right)^{-1} = \left\langle \left((\mathbb{A}(\mathbf{x}) - \mathbb{A}_0)^{-1} + \Gamma_{\mathbb{A}_0}(\mathbf{n}) \right)^{-1} \right\rangle. \quad (2.23)$$

Here, the inverse is taken on the space M^+ in which $\bar{\mathbb{A}} \in M^+$ lives, $\mathbb{A} : Y \rightarrow M^+$ denotes the field of the phase wise primal or dual material properties

$$\mathbb{A} : Y \rightarrow M^+, \quad \mathbf{x} \mapsto \begin{cases} \mathbb{A}_1 & \text{if } \mathbf{x} \in Y_1, \\ \mathbb{A}_2 & \text{if } \mathbf{x} \in Y_2, \end{cases} \quad (2.24)$$

and $\mathbb{A}_0 \in M^+$ refers to an arbitrary reference material tensor such that the term $(\mathbb{A}(\mathbf{x}) - \mathbb{A}_0)$ is invertible. Also, the operator $\Gamma_{\mathbb{A}_0}(\mathbf{n}) \in (\mathbb{R}^3)^{\otimes 4}$ is defined as

$$\Gamma_{\mathbb{A}_0}(\mathbf{n}) = \Gamma_{\mathbb{I}}(\mathbf{n}) [\Gamma_{\mathbb{I}}(\mathbf{n}) \mathbb{A}_0 \Gamma_{\mathbb{I}}(\mathbf{n})]^\dagger \Gamma_{\mathbb{I}}(\mathbf{n}), \quad (2.25)$$

where $(\cdot)^\dagger$ stands for the Moore–Penrose pseudoinverse, and the operators $\Gamma_{\mathbb{A}_0}(\mathbf{n})$ and $\Gamma_{\mathbb{I}}(\mathbf{n})$ project onto the same subspace with respect to different inner products. More specifically, the operator $\Gamma_{\mathbb{A}_0}(\mathbf{n})$ is an orthogonal projector with respect to the \mathbb{A}_0 -weighted inner product

$$\langle \mathbf{X}, \mathbf{X} \rangle_{\mathbb{A}_0} = \mathbf{X} \cdot \mathbb{A}_0[\mathbf{X}], \quad \mathbf{X} \in \text{Sym}(3), \quad (2.26)$$

and the operator $\Gamma_{\mathbb{I}}(\mathbf{n})$ is an orthogonal projector with respect to the Frobenius inner product

$$\langle \mathbf{X}, \mathbf{X} \rangle_{\text{F}} = \mathbf{X} \cdot \mathbb{I}[\mathbf{X}] = \mathbf{X} \cdot \mathbf{X}, \quad \mathbf{X} \in \text{Sym}(3), \quad (2.27)$$

where $\mathbb{I} \in (\mathbb{R}^3)^{\otimes 4}$ denotes the fourth order identity tensor. The operator $\Gamma_{\mathbb{I}}(\mathbf{n})$ encodes restrictions imposed by the periodicity of the laminate, the perfect bonding of the phases, the momentum balance (2.11), and the constitutive equation (2.19). Depending on whether we wish to compute the effective primal or the effective dual properties of the laminate, a different operator $\Gamma_{\mathbb{I}}(\mathbf{n})$ is required. For the homogenization of the primal effective properties, i.e., $\bar{\mathbb{A}} = \bar{\mathbb{M}}$, the operator $\Gamma_{\mathbb{I}}(\mathbf{n})$ equals the operator $\Gamma_1^{\text{co}}(\mathbf{n})$. For the homogenization of the dual effective properties, i.e., $\bar{\mathbb{A}} = \bar{\mathbb{K}}$, the operator $\Gamma_{\mathbb{I}}(\mathbf{n})$ equals the operator $\Gamma_2^{\text{co}}(\mathbf{n})$. The operators Γ_1^{co} and Γ_2^{co} , are defined through their action on a second order tensor $\mathbf{X} \in \text{Sym}(3)$

$$\Gamma_1^{\text{co}}(\mathbf{n})[\mathbf{X}] = 2(\mathbf{X}\mathbf{n}) \otimes_s \mathbf{n} - (\mathbf{n} \cdot \mathbf{X}\mathbf{n})\mathbf{n} \otimes \mathbf{n} \quad \text{and} \quad \Gamma_2^{\text{co}}(\mathbf{n})[\mathbf{X}] = \mathbf{X} - \Gamma_1^{\text{co}}(\mathbf{n})\mathbf{X}, \quad (2.28)$$

where \otimes_s denotes the symmetrized dyadic product. The operators Γ_1^{co} and Γ_2^{co} project onto the subspaces

$$\mathcal{E}^{\text{co}} = \{ \text{Sym}(3) \ni \mathbf{X} = \mathbf{d} \otimes \mathbf{n} + \mathbf{n} \otimes \mathbf{d} \mid \mathbf{d} \in \mathbb{R}^3 \} \quad \text{and} \quad \mathcal{S}^{\text{co}} = \{ \text{Sym}(3) \ni \mathbf{X} \mid \mathbf{X}\mathbf{n} = \mathbf{0} \}, \quad (2.29)$$

and arise from the fact that the jumps of the field $[[\nabla^s \mathbf{w}]] \in \mathcal{E}^{\text{co}}$

$$[[\nabla^s \mathbf{w}]] = [[\nabla \mathbf{w} \mathbf{n}]] \otimes_s \mathbf{n}, \quad (2.30)$$

and the jump of the stress $\llbracket \boldsymbol{\sigma} \rrbracket \in \mathcal{S}^{\text{co}}$ live on mutually orthogonal subspaces [69, §9], because it holds that

$$\llbracket \boldsymbol{\sigma} \mathbf{n} \rrbracket = \mathbf{0}. \quad (2.31)$$

Here, we define the jump $\llbracket q \rrbracket$ of a quantity q across a phase boundary with normal vector \mathbf{n} as

$$\llbracket q \rrbracket = q^+ - q^-, \quad (2.32)$$

where q^+ and q^- denote the outer and inner limits of the quantity q with regard to the outside facing normal vector \mathbf{n} , respectively.

Interestingly, the constitutive equations for kinematically unconstrained linear elastic solids and linearly viscous fluids share the same structure, see equation (2.19). Additionally, equations (2.30) and (2.31) are satisfied for layered emulsions by definition, because there is no slip between the phases, and the momentum balance (2.11) is satisfied. Thus, the homogenization problem for the considered layered emulsions has the same structure as the homogenization problem for laminates. As a result, the effective properties $\bar{\mathbb{A}} \in \mathbb{M}^+$ of a two-phase layered emulsion of kinematically unconstrained materials $m_1, m_2 \in \mathcal{M}$ can be computed with equation (2.23). If the kinematic field \mathbf{w} is solenoidal such that the incompressible balance of mass (2.14) is satisfied, it follows from equation (2.30) that

$$\llbracket \nabla^s \mathbf{w} \mathbf{n} \rrbracket \cdot \mathbf{n} = 0. \quad (2.33)$$

Also, if the materials $m_1, m_2 \in \mathcal{M}$ are incompressible, it follows from equations (2.21) and (2.31) that

$$\llbracket \boldsymbol{\sigma} \mathbf{n} \rrbracket = \mathbf{0} \quad \iff \quad \llbracket \boldsymbol{\tau} \mathbf{n} \rrbracket = \llbracket p \rrbracket \mathbf{n}. \quad (2.34)$$

Therefore, the jumps $\llbracket \nabla^s \mathbf{w} \rrbracket \in \mathcal{E}^{\text{ico}}$ and $\llbracket \boldsymbol{\sigma} \rrbracket \in \mathcal{S}^{\text{ico}}$ live in the mutually orthogonal spaces

$$\mathcal{E}^{\text{ico}} = \{ \text{Sym}_0(3) \ni \mathbf{X} = 2 \mathbf{d} \otimes_s \mathbf{n} - 2(\mathbf{d} \cdot \mathbf{n}) \mathbf{n} \otimes \mathbf{n} \mid \mathbf{d} \in \mathbb{R}^3 \} \quad (2.35)$$

and

$$\mathcal{S}^{\text{ico}} = \{ \text{Sym}_0(3) \ni \mathbf{X} \mid \mathbf{X} \mathbf{n} = a \mathbf{n}, \quad a \in \mathbb{R} \}. \quad (2.36)$$

The two operators $\Gamma_1^{\text{ico}}(\mathbf{n})$ and $\Gamma_2^{\text{ico}}(\mathbf{n})$, defined through their action on a traceless second order tensor $\mathbf{X} \in \text{Sym}_0(3)$,

$$\Gamma_1^{\text{ico}}(\mathbf{n})[\mathbf{X}] = 2(\mathbf{X} \mathbf{n}) \otimes_s \mathbf{n} - 2(\mathbf{n} \cdot \mathbf{X} \mathbf{n}) \mathbf{n} \otimes \mathbf{n} \quad \text{and} \quad \Gamma_2^{\text{ico}}(\mathbf{n})[\mathbf{X}] = \mathbf{X} - \Gamma_2^{\text{ico}}(\mathbf{n})[\mathbf{X}], \quad (2.37)$$

project onto the spaces \mathcal{E}^{ico} and \mathcal{S}^{ico} , respectively. Consequently, the procedure detailed in Milton [69] can be used to compute the effective properties $\bar{\mathbb{A}} \in \mathbb{M}_0^+$ of a layered material with incompressible constituents. In this context the homogenization equation (2.23) applies if the property field $\mathbb{A} : Y \rightarrow \mathbb{M}_0^+$, the reference properties $\mathbb{A}_0 \in \mathbb{M}_0^+$, and the operator $\Gamma_{\mathbb{I}}(\mathbf{n}) \in (\Gamma_1^{\text{ico}}(\mathbf{n}), \Gamma_2^{\text{ico}}(\mathbf{n}))$ are selected based on whether the tensor $\bar{\mathbb{A}}$ represents primal or dual effective properties. In summary, for a layered material consisting of linear materials $m_1, m_2 \in \mathcal{M}$, the effective material properties $(\bar{\mathbb{M}}, \bar{\mathbb{K}}) \in \{(\mathbb{M}^+)^2, (\mathbb{M}_0^+)^2\}$ can be computed with the homogenization equation (2.23). The choice of the operator $\Gamma_{\mathbb{I}}(\mathbf{n})$ depends on whether the phases are compressible or incompressible, and whether the primal or dual effective tensors are sought.

2.3 Coated layered materials

Because we are interested in building FDMNs for suspensions of rigid particles, the architecture of the FDMN should be capable of handling infinitely viscous, i.e., rigid, phases. In this section, we leverage the homogenization equation (2.23) to study the homogenization of repeatedly layered materials in the

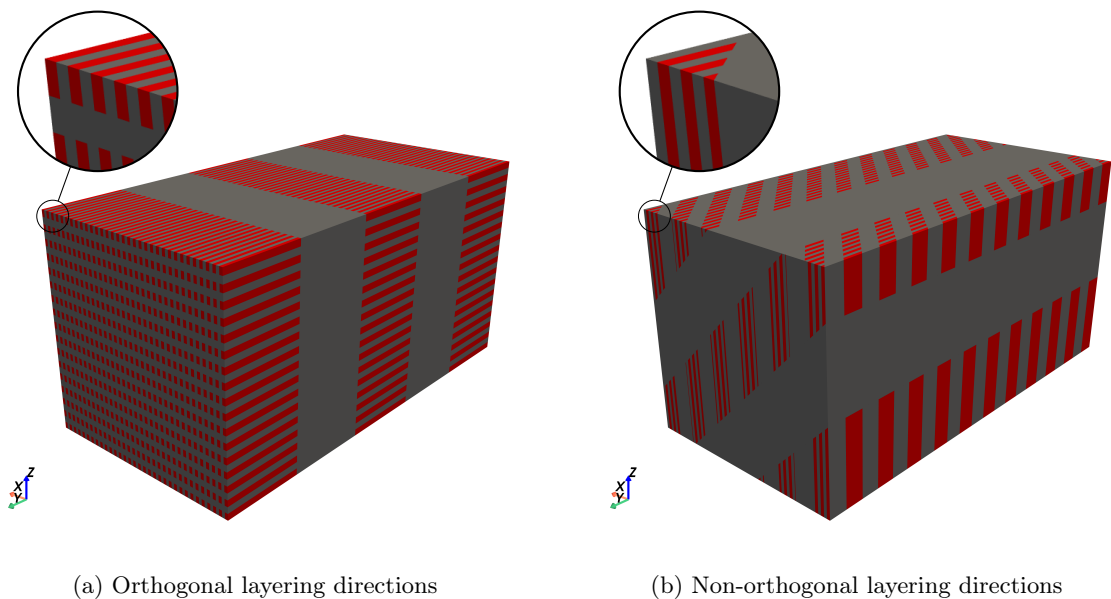


Figure 1: Rank-three, coated layered materials with orthogonal layering directions (a), and non-orthogonal layering directions (b). The core material is shown in red and the coating material is shown in gray. We hint at the separation of length scales between the material layers through our choice of the layer thicknesses.

presence of rigid phases. We define and use the term *rank* of a layered material in the following to better distinguish between the possible ways to construct layered materials. The rank $R \in \mathbb{N}_{\geq 0}$ of a hierarchical, layered material defines the number of layering steps that are needed to construct the material using layering directions $\mathbf{n}_r \in \mathcal{S}^2$, such that the index r starts at one and ends at R , i.e., $r \in \{1, \dots, R\}$. By definition, a rank-0 layered material is simply a single phase material without any layering. Also, the materials that are layered at each layering step need not be the same. For example, let the first layer in a rank-2 layered material consist of the materials m_1 and m_2 . Then, the second layer may consist of the materials m_1 and m_2 in the form of the first layer, and a third material m_3 .

Rank-one two-phase layered materials are unsuitable as DMN building blocks in the case of infinite material contrast, because their effective properties are always singular if one phase is singular. In search of a building block capable of handling rigid phases, we study the effective properties of a particular type of layered material following the terminology and the analytical approach detailed by Milton [69, §9]. We refer to this particular type of layered materials as coated layered materials (CLMs). To construct a CLM, one material m_2 , called the coating, is repeatedly layered onto another material m_1 , called the core. The layering process is divided into multiple steps, such that the r -th layering step is applied in direction \mathbf{n}_r , and the total number of layering steps equals the rank R of the CLM. As an example, two rank-three CLMs are depicted in Figure 1, where the layering directions $\mathbf{n}_r \in \mathcal{N}_1$ of the material shown in Figure 1(a) are

$$\mathcal{N}_1 = \{(1, 0, 0)_{\{e_i\}}, (0, 0, 1)_{\{e_i\}}, (0, 1, 0)_{\{e_i\}}\}, \quad (2.38)$$

and the layering directions $\mathbf{n}_r \in \mathcal{N}_2$ of the material shown in Figure 1(b) are

$$\mathcal{N}_2 = \left\{ (1, 0, 0)_{\{e_i\}}, \frac{1}{\sqrt{2}} (1, 1, 0)_{\{e_i\}}, \frac{1}{\sqrt{2}} (1, 0, 1)_{\{e_i\}} \right\}. \quad (2.39)$$

As described, the gray coating material m_2 is repeatedly applied in layers, such that for $r > 1$, the r -th sub layer of the rank-three CLM is constructed by layering a rank- $(r - 1)$ layered material with

the coating material m_2 . By definition, the 0-th sub layer of the rank-three CLM is purely made of the core material m_1 . We wish to compute the effective properties $\bar{\mathbb{A}}$ of a coated layered material by repeatedly applying the homogenization equation (2.23). For the recursive application of the rank-one homogenization formula (2.23) to be valid, the phases at each homogenization step must be homogeneous on the length scale of the respective layering step. This requires a separation of length scales, in the sense that the thickness δ_r of the material sections in the rank- r sub layer is drastically smaller than the thickness δ_{r+1} of the material sections in the next sub layer, i.e., $\delta_r \ll \delta_{r+1}$. In Figure 1, we hint at this separation of length scales between the material layers through our choice of the layer thicknesses. Nonetheless, we retain a visible degree of inhomogeneity, so that the layer structures can be distinguished for illustration purposes.

Before we repeatedly apply equation (2.23) to derive an expression for the effective properties $\bar{\mathbb{A}}$, we first simplify the expression (2.23) for the case at hand. We let the reference material properties \mathbb{A}_0 in equation (2.23) approach the properties \mathbb{A}_2 of the coating material m_2 , resulting in the equation [69, §9]

$$(1 - f_2)(\bar{\mathbb{A}} - \mathbb{A}_2)^{-1} = (\mathbb{A}_1 - \mathbb{A}_2)^{-1} + f_2 \Gamma_{\mathbb{A}_2}(\mathbf{n}). \quad (2.40)$$

Here, the coating material m_2 must not be rigid or a void, the tensor $(\mathbb{A}_1 - \mathbb{A}_2)$ must be invertible, and f_2 denotes the volume fraction of the coating material m_2 . Also, the fourth order tensor $\Gamma_{\mathbb{A}_2}(\mathbf{n}_r) \in (\mathbb{R}^3)^{\otimes 4}$ is defined by equation (2.25) as

$$\Gamma_{\mathbb{A}_2}(\mathbf{n}_r) = \mathbb{I}_{\mathbb{I}}(\mathbf{n}_r) [\mathbb{I}_{\mathbb{I}}(\mathbf{n}_r) \mathbb{A}_2 \mathbb{I}_{\mathbb{I}}(\mathbf{n}_r)]^\dagger \mathbb{I}_{\mathbb{I}}(\mathbf{n}_r), \quad (2.41)$$

where the inverse is taken on the subspace onto which $\mathbb{I}_{\mathbb{I}}$ projects. To compute the effective properties $\bar{\mathbb{A}}$ of a rank- R CLM, we recursively apply equation (2.40) for the effective material properties of rank-one layered materials, such that [69, §9]

$$(1 - f_2)(\bar{\mathbb{A}} - \mathbb{A}_2)^{-1} = (\mathbb{A}_1 - \mathbb{A}_2)^{-1} + f_2 \sum_{r=1}^R c_r \Gamma_{\mathbb{A}_2}(\mathbf{n}_r). \quad (2.42)$$

Here, the scalars c_r are computed from the volume fractions $f_1^{(r)}$ of the core material m_1 in the rank- r sub layer of the rank-three CLM, such that

$$c_r = \frac{f_1^{(r-1)} - f_1^{(r)}}{f_2}, \quad (2.43)$$

i.e., the properties

$$\sum_{r=1}^R c_r = 1 \quad \text{and} \quad c_r > 0, \quad (2.44)$$

hold. Because the rank-0 sub layer consists solely of the core material m_1 by definition, the volume fraction $f^{(0)} = 1$ is one. Equation (2.42) is essential to compute the effective properties of layered materials with infinite material contrast, and thus for the treatment of such materials using a DMN architecture. In Appendix A, we employ equation (2.42) to study the conditions under which the effective properties $\bar{\mathbb{A}}$ of a CLM are singular when the core material m_1 is rigid. With the objective of applying FDMNs to suspensions of rigid fibers in mind, we summarize the results pertaining to rank- R CLMs with a *rigid* core material m_1 and an *incompressible* coating material m_2 with the following statements.

1. The effective properties $\bar{\mathbb{A}}$ of a CLM of rank $R < 3$ are always singular.
2. For rank-3 CLMs, the effective properties $\bar{\mathbb{A}}$ are singular if at least one layering direction is orthogonal to two other layering directions, or if at least two layering directions are collinear.

3. Rank-3 CLMs with mutually non-orthogonal and mutually non-collinear layering directions $\mathbf{n}_1, \mathbf{n}_2$, and \mathbf{n}_3 have non-singular effective properties. Thus, in the context of this article, we require

$$0 < |\mathbf{n}_1 \cdot \mathbf{n}_2| < 1, \quad 0 < |\mathbf{n}_1 \cdot \mathbf{n}_3| < 1, \quad 0 < |\mathbf{n}_2 \cdot \mathbf{n}_3| < 1. \quad (2.45)$$

The statements 1-3 are of critical importance for the treatment of incompressible suspensions of rigid particles using a DMN architecture. It follows that CLMs with an incompressible coating material and rigid core material should be at least of rank $R = 3$ and have non-collinear and mutually non-orthogonal layering directions to be non-singular. Therefore, we leverage such non-singular-singular rank-3 CLMs in the FDMN architecture to treat suspensions of rigid fibers, as we explain in section 3.2.

3 Identifying deep material networks for suspensions of rigid fibers

3.1 Architecture of direct deep material networks

Because the FDMN architecture extends the (direct) DMN framework, we briefly summarize the direct DMN architecture in this section, before presenting the FDMN architecture in the next section 3.2. For in depth discussions and explanations of the direct DMN architecture, we refer the reader to articles by Gajek et al. [46, 54, 59]. A two-phase direct DMN is defined as a perfect binary tree, consisting of two-phase laminates \mathcal{B}_k^i as nodes, see Figure 2(a). The laminates \mathcal{B}_k^i are defined by a single lamination direction \mathbf{n}_k^i and two volume fractions $c_{k,1}^1$ and $c_{k,1}^2$. The DMN tree is ordered, rooted and has depth K . We use the letter $k = 1, \dots, K$ to denote the depth of a node and the letter $i = 1, \dots, 2^{k-1}$ to indicate the horizontal position of a node in the respective layer. We parametrize a direct DMN by the two

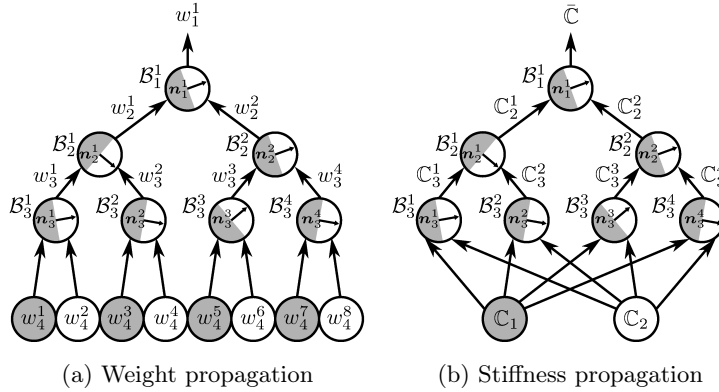


Figure 2: Weight and stiffness propagation (from the bottom to the top) in a two-phase direct DMN [46] of depth $K = 3$, by Gajek et al. [59, Fig. 1], licensed under CC BY 4.0

vectors $\underline{n} \in (\mathbb{R}^3)^{2^K - 1}$

$$\underline{n} = (\mathbf{n}_K^1, \dots, \mathbf{n}_K^{2^{K-1}}, \mathbf{n}_{K-1}^1, \dots, \mathbf{n}_{K-1}^{2^{K-2}}, \dots, \mathbf{n}_1^1), \quad (3.1)$$

and $\underline{w} \in \mathbb{R}^{2^K}$

$$\underline{w} = (w_{K+1}^1, \dots, w_{K+1}^{2^K}). \quad (3.2)$$

Instead of the laminate volume fractions, the direct DMN is parametrized in terms of the weights w_{K+1}^i to improve numerical stability during the training process [52, 53]. The i -th weight in the k -th layer is computed from the pairwise summation of the weights in the previous layer $k + 1$, see Figure 2(a), such that

$$w_k^i = w_{k+1}^{2i-1} + w_{k+1}^{2i}, \quad (3.3)$$

and the volume fractions $c_{k,1}^i$ and $c_{k,2}^i$ follow from

$$c_{k,1}^i = \frac{w_{k+1}^{2i-1}}{w_{k+1}^{2i-1} + w_{k+1}^{2i}}, \quad \text{and} \quad c_{k,2}^i = 1 - c_{k,1}^i. \quad (3.4)$$

Additionally, the weights w_{K+1}^i need to be positive and sum to unity, such that

$$w_{K+1}^i \geq 0 \quad \text{and} \quad \sum_i^{2^K} w_{K+1}^i = 1. \quad (3.5)$$

The vectors \underline{n} and \underline{w} fully parametrize a direct DMN of depth K and are identified by fitting the linear homogenization function of the DMN to the linear homogenization function of the microstructure of interest. The fitting process is carried out by using supervised machine learning, and we refer to this process as *offline training*. To evaluate the linear homogenization function of the DMN during the offline training, input stiffness pairs are propagated through the network of homogenization blocks \mathcal{B}_k^i , see Figure 2(b). Consequently, if the stiffness \mathbb{C}_k^i of a homogenization block \mathcal{B}_k^i is singular, this singular stiffness can propagate through the whole DMN, which is undesirable for the offline training. Once the parameter vectors \underline{n} and \underline{w} are known, they remain unchanged and are used in the *online evaluation* to predict the non-linear response of the studied material. In sections 3.4, 4.2, and 3.5, we discuss the offline training and the online evaluation for the proposed FDMN architecture.

3.2 Architecture of flexible deep material networks

With the results of the previous sections 2.1-2.3 at hand, we present an extended DMN architecture that is able to treat fluid phases and infinite material contrast. Compared to the architecture of (direct) DMNs shown in Figure 2, the lowest layer of laminates is replaced by a layer of rank- R CLMs \mathcal{C}_R , see Figure 3. The rank R of the CLM \mathcal{C}_R and the restrictions on its layering directions \mathbf{n}_r are problem dependent, and

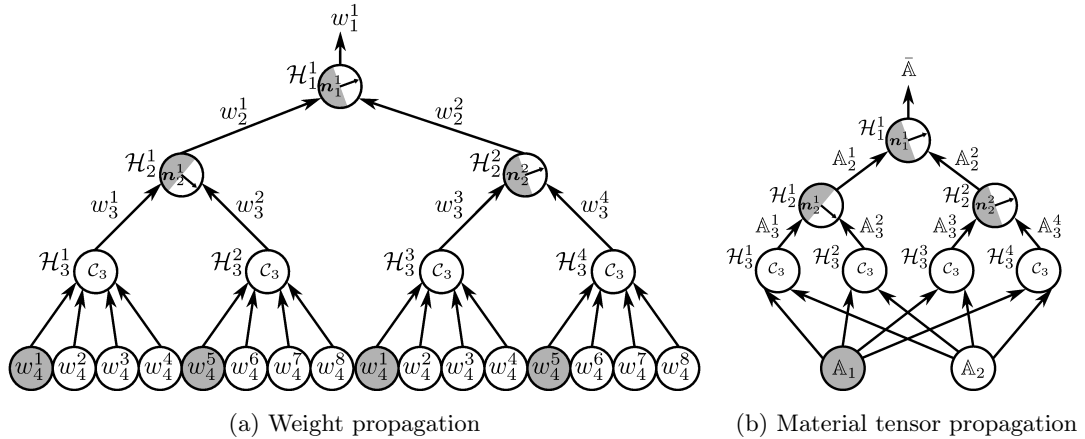


Figure 3: Weight and material property propagation (from the bottom to the top) in a two-phase FDMN [46] of depth $K = 3$ with rank-3 CLMs

chosen such that the non-singularity condition (5.11) is satisfied. This guarantees that only non-singular material tensors \mathbb{A}_k^i are propagated through the network. If all phases are kinematically unconstrained, solid, and non-singular, rank-1 CLMs can be employed to recover the direct DMN architecture. However, in the case of incompressible suspensions of rigid particles, the CLMs are of rank $R = 3$ and have mutually non-collinear and non-orthogonal layering directions \mathbf{n}_r , as per statements 1-3. Additionally,

the homogenization blocks \mathcal{H}_k^i implement the general homogenization function defined by equation (2.23) in which the projector function \mathbb{F}_Γ depends on the physics of the investigated problem. This allows the treatment of composites consisting of linear materials $m \in \mathcal{M}$, including incompressible linearly viscous fluids. For problems involving two-phase materials, $R + 1$ weights and two materials are assigned to each CLM. The number of layering directions N_n and the number of input weights N_w in a two-phase FDMN of depth K with rank- R CLMs are

$$N_n = 2^{K-1}(R + 1) - 1, \quad N_w = 2^{K-1}(R + 1). \quad (3.6)$$

As an example, Figures 3(a) and 3(b) show the weight and material property propagation of a two-phase FDMN of depth $K = 3$ with two-phase CLMs of rank $R = 3$ as bottom layer. Of the four weights of a rank-3 CLM, one is associated with the core material m_1 , and three are associated with the coating material m_2 . This doubles the number of weights for an FDMN with rank-3 CLMs as compared to a DMN of the same depth K . Additionally, each rank-3 CLM block \mathcal{C}_3 has three layering directions \mathbf{n}_r instead of one layering direction like rank-one laminates. To reduce the number of free parameters and ensure the CLMs are non-singular, the relative angles between the layering directions \mathbf{n}_r are fixed, while their joint orientation in space is determined through the offline training, as we explain in section 3.4 in more detail. Because CLMs are based on the repeated layering of rank-one layered materials, an FDMN of depth K can be considered to be a special case of a (direct) DMN of depth $K + (R - 1)$ with generalized homogenization blocks. Then, a CLM represents a subtree of the DMN of depth $K + (R - 1)$, in which the weights w_k^i of certain phases are set to zero, such that a CLM emerges, see Figure 4. In

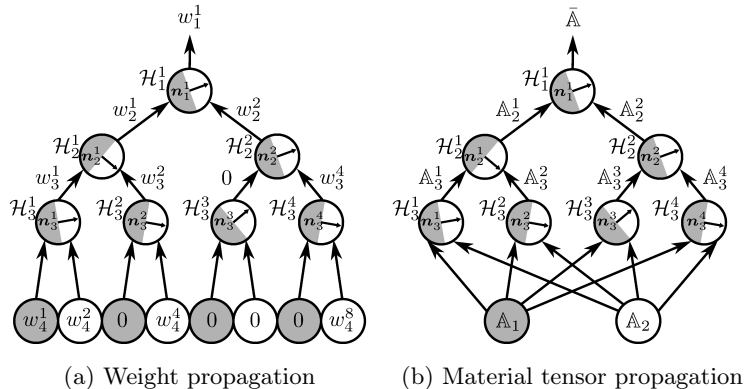


Figure 4: Weight and material property propagation (from the bottom to the top) in a two-phase DMN of depth $K = 3$, representing a two-phase rank-3 CLM

particular, except for one phase, the weights associated with the singular core material m_1 are set to zero. Additionally, R weights associated with the non-singular coating material m_2 must be non-zero, such that the rank R of the CLM is maintained. Technically, (direct) DMNs are therefore able to treat infinite material contrast intrinsically. However, the weights w_k^i need to be identified during the offline training, and might not always have appropriate values to generate CLMs with the required rank, such that singular material tensors \mathbb{A}_k^i might propagate through the whole DMN. Also, if the layering normals are not chosen appropriately, the singular material properties may propagate through the whole DMN as well. Controlling the weights and normals via the implementation of the CLM blocks instead of learning them is therefore preferable to prevent singularities during the offline training. Furthermore, FDMNs of depth K have fewer free parameters compared to equivalent DMNs of depth $K + R - 1$, which aids in the offline training as well.

Hypothetically, the presented FDMN architecture could be applied to problems with more than two phases as well. Let N_R denote the number of non-singular phases and N_S denote the number of singular phases. Then, for each singular phase, the FDMN needs to contain at least one CLM to which the phase is assigned, and which has non-singular effective properties. This requires a minimum of N_S CLMs. Additionally, the coatings of the CLMs can be constructed by mixing the non-singular phases, possibly by constructing N_R -phase layered materials. However, the application of FDMNs to materials with voids or more than two phases is beyond the scope of this article, because we focus on suspensions of rigid fibers.

3.3 Material sampling

For materials with solid phases, DMNs are trained by sampling the linear elastic homogenization function of the microstructure of interest with randomly generated input materials [46, 52, 53, 59], and fitting the DMN parameters to replicate the desired homogenization function. Similarly, in the case of rigid particles suspended in viscous media, we train FDMNs to learn the linear viscous homogenization function with the goal of predicting non-linear viscous behavior. Consequently, we sample the linear viscous homogenization function by using randomly generated, linearly viscous input materials. We base our sampling strategy on the approach used by Gajek et al. [46]. In the article by Gajek et al. [46] on glass fiber reinforced polyamide composites, the authors chose the stiffness samples for the fiber material to be isotropic, and the stiffness samples for to the polyamide matrix to be transversely isotropic. This strategy leads to a smaller sample space compared to sampling orthotropic stiffnesses for both the fiber and the matrix materials, as suggested by Liu et al. [52, 53]. To reduce the computational cost of sampling even further for the considered case of fiber suspension, we only generate sample viscosities for the matrix material and consider the suspended fibers to be rigid in all computations. To generate samples for the matrix material, we follow Gajek et al. [46] and choose the sample viscosity \mathbb{V}^s pertaining to the s -th sample to be transversely isotropic, such that

$$\mathbb{V}^s = 2\eta_2 (\mathbb{P}_2 - g\mathbf{A}'(\underline{a}) \otimes \mathbf{A}'(\underline{a})), \quad (3.7)$$

where the scalar $g \in [0, 1)$ defines the magnitude of the perturbation by the unitary and deviatoric tensor $\mathbf{A}'(\underline{a}) \in \text{Sym}_0(3)$, the vector $\underline{a} \in \mathbb{R}^4$ collects four angles, and we consider the scalar viscosities

$$\eta_2 = 10^p \text{GPa}, \quad p \in [-3, 3]. \quad (3.8)$$

For a fiber reinforced polyamide, Gajek et al. [46] employed an ansatz of the form (3.7) to sample the material tangents of a J2-elastoplastic matrix material. Similarly, with the objective of applying FDMNs to fiber suspensions with a shear-thinning polyamide matrix as detailed in section 4.1, we use equation (3.7) to sample the material tangents of a Cross-type (4.4) matrix material. The tensor function \mathbf{A}' is defined by an eigenvalue decomposition [46]

$$\mathbf{A}' : \mathbb{R}^4 \rightarrow \text{Sym}_0(3), \quad (3.9)$$

$$(a_1, a_2, a_3, a_4)^\top \mapsto \mathbf{Q}(a_2, a_3, a_4)\mathbf{A}(a_1)\mathbf{Q}(a_2, a_3, a_4)^\top, \quad (3.10)$$

into the orthogonal tensor $\mathbf{Q}(a_2, a_3, a_4)$ and a diagonal tensor $\mathbf{A}(a_1)$ in terms of the vector $\underline{a} = (a_1, a_2, a_3, a_4)^\top$. The tensor $\mathbf{A}(a_1)$ is constructed from the angle a_1 via [46]

$$\mathbf{A} = \frac{1}{\sqrt{\frac{\xi_1+1}{2\xi_1+1}}} \text{diag} \left(\xi_2 \cos(a_1), \xi_2 \sin(a_1), \frac{1}{\sqrt{2}} \right), \quad (3.11)$$

$$\xi_1 = \cos(a_1) \sin(a_1), \quad \xi_2 = \frac{-\sqrt{2}}{2 \cos(a_1) + 2 \sin(a_1)}, \quad (3.12)$$

and the tensor $\mathbf{Q}(a_2, a_3, a_4)$ represents a rotation around the direction \mathbf{n} , such that

$$\mathbf{Q}(a_2, a_3, a_4) : \mathbb{R}^3 \rightarrow \mathbb{R}^3, \quad \mathbf{x} \mapsto \cos(a_2) \mathbf{x} + \sin(a_2) \mathbf{n} \times \mathbf{x} + (1 - \cos(a_2))(\mathbf{n} \cdot \mathbf{x})\mathbf{n}, \quad (3.13)$$

$$\mathbf{n} = \sin(a_3) \cos(a_4) \mathbf{e}_1 + \sin(a_3) \sin(a_4) \mathbf{e}_2 + \cos(a_3) \mathbf{e}_3. \quad (3.14)$$

Here, the operator **diag** constructs a second order tensor in the standard basis \mathbf{e}_i of \mathbb{R}^3 , and the components of the vector \underline{a} live on the intervals

$$a_1 \in [0, 2\pi], \quad a_2 - \sin(a_2) \in [0, \pi], \quad a_3 \in [0, \pi], \quad a_4 \in [0, 2\pi]. \quad (3.15)$$

We sample the space of the variables p and \underline{a} using the scrambled Sobol sequence [74, 75], and employ an FFT-based computational procedure to compute the resulting effective viscosities \bar{V}^s [17, 38], see section (4).

3.4 Offline training

Using the material sampling procedure described in the previous section 3.3, we wish to optimize the parameters of the FDMN with regard to the training data set. For the case of rigid fibers suspended in viscous media, we consider FDMNs with rank-3 CLMs as bottom layer, which satisfy the requirements derived in section A.2. We collect all layering directions of the FDMN in a vector

$$\underline{n} = (\mathbf{n}_K^1, \dots, \mathbf{n}_K^{3(2^{K-1})}, \mathbf{n}_{K-1}^1, \dots, \mathbf{n}_{K-1}^{2^{K-2}}, \dots, \mathbf{n}_2^1, \mathbf{n}_2^2, \mathbf{n}_1^1), \quad (3.16)$$

where we used the fact that the k -th layer contains 2^{k-1} normals if $k < K$, and the K -th layer contains $3(2^{K-1})$ normals. Because the homogenization blocks in the K -th layer are rank-three CLMs, the number of normals is different from the other layers. Each normal \mathbf{n}_k^i in the k -th layer for $k < K$ is constructed using two angles a_k^i and b_k^i via

$$\mathbf{n}_k^i = \sin(b_k^i) \cos(a_k^i) \mathbf{e}_1 + \sin(b_k^i) \sin(a_k^i) \mathbf{e}_2 + \cos(b_k^i) \mathbf{e}_3. \quad (3.17)$$

However, for the normals \mathbf{n}_K^i in the K -th layer, the procedure is different. To avoid singular effective properties during the evaluation of the FDMN in accordance with the discussion in sections 2.3 and A.2, we ensure that the three layering normals of a rank-three CLM block are not mutually non-orthogonal and mutually non-collinear as follows. First, for each rank-three CLM block \mathcal{C}_3^i , we compute the components Q_{op}^i of the orthogonal tensor \mathbf{Q}^i in the standard basis $\{\mathbf{e}_i\}$ using three Euler angles $c_K^i, d_K^i, e_K^i \in [0, 2\pi]$ via

$$Q_{op}^i = \begin{bmatrix} 1 & 0 & 0 \\ 0 & \cos(c_K^i) & -\sin(c_K^i) \\ 0 & \sin(c_K^i) & \cos(c_K^i) \end{bmatrix} \begin{bmatrix} \cos(d_K^i) & 0 & \sin(d_K^i) \\ 0 & 1 & 0 \\ -\sin(d_K^i) & 0 & \cos(d_K^i) \end{bmatrix} \begin{bmatrix} \cos(e_K^i) & -\sin(e_K^i) & 0 \\ \sin(e_K^i) & \cos(e_K^i) & 0 \\ 0 & 0 & 1 \end{bmatrix}. \quad (3.18)$$

Then, we compute the layering directions $\mathbf{n}_K^{3(i-1)+1}, \mathbf{n}_K^{3(i-1)+2}, \mathbf{n}_K^{3(i-1)+3}$ of the rank-three CLM \mathcal{C}_3^i via

$$\mathbf{n}_K^{3(i-1)+1} = \mathbf{q}_1^i, \quad \mathbf{n}_K^{3(i-1)+2} = \frac{1}{\sqrt{2}} (\mathbf{q}_1^i + \mathbf{q}_2^i), \quad \mathbf{n}_K^{3(i-1)+3} = \frac{1}{\sqrt{2}} (\mathbf{q}_1^i + \mathbf{q}_3^i), \quad (3.19)$$

where $\mathbf{q}_1^i, \mathbf{q}_2^i$, and \mathbf{q}_3^i are the first, second, and third column vectors of the tensor \mathbf{Q}^i in the standard basis \mathbf{e}_i , respectively. This leads to a total of N_α angles with

$$N_\alpha = 5(2^{K-1}) - 2. \quad (3.20)$$

The angles between the layering directions are fixed for each CLM \mathcal{C}_3 , but the three layering directions are rotated together during training. Other procedures than the one presented here are viable as well, as long as the constructed vectors $\mathbf{n}_K^{3(i-1)+1}$, $\mathbf{n}_K^{3(i-1)+2}$, and $\mathbf{n}_K^{3(i-1)+3}$ are mutually non-collinear and non-orthogonal. Alternatively, one could parametrize each of the three layering directions $\mathbf{n}_K^{3(i-1)+1}$, $\mathbf{n}_K^{3(i-1)+2}$, and $\mathbf{n}_K^{3(i-1)+3}$ with two angles each, and identify the angles independently. Then, the effective properties of the CLM \mathcal{C}_3^i are non-singular almost surely, because the probability of any two of the three layering directions being collinear or one vector being orthogonal to the other two is zero. However, parametrizing each of the three layering directions with two angles requires twice the amount of angles in the CLM layer of the FDMN as compared to the presented procedure.

To define the linear homogenization function of the FDMN, we collect all N_α angles of the layering directions in the vector $\underline{\alpha}$

$$\underline{\alpha} = (c_K^1, d_K^1, e_K^1, \dots, c_K^{3(2^{K-1})}, d_K^{3(2^{K-1})}, e_K^{3(2^{K-1})}, a_{K-1}^1, b_{K-1}^1, \dots, a_{K-1}^{2^{K-2}}, b_{K-1}^{2^{K-2}}, \dots, a_1^1, b_1^1), \quad (3.21)$$

and collect all N_w input weights of the FDMN in the vector

$$\underline{w} = (w_{K+1}^1, \dots, w_{K+1}^{N_w}). \quad (3.22)$$

We follow Gajek et al. [54] and define the loss function $\mathcal{L} : \mathbb{R}^{\otimes N_\alpha} \times \mathbb{R}^{\otimes N_w} \rightarrow \mathbb{R}$ in terms of the linear homogenization function $\mathcal{DMN}_L : \mathcal{A} \times \mathcal{A} \times \mathbb{R}^{\otimes N_\alpha} \times \mathbb{R}^{\otimes N_w} \rightarrow \mathcal{A}$ of the FDMN as

$$\mathcal{L}(\underline{\alpha}, \underline{w}) = \frac{1}{N_b} \sqrt[q]{\sum_{s=1}^{N_b} \left(\frac{\|\bar{\mathbb{A}}^s - \mathcal{DMN}_L(\mathbb{A}_1^s, \mathbb{A}_2^s, \underline{\alpha}, \underline{w})\|_p}{\|\bar{\mathbb{A}}^s\|_p} \right)^q} + \lambda \left(\sum_{i=1}^{N_w} w_{K+1}^i - 1 \right)^2, \quad (3.23)$$

where N_b is the number of samples, $\mathbb{A}_1^s, \mathbb{A}_2^s \in \mathcal{A}$ denote the material tensors of the phases of a sample, and $\bar{\mathbb{A}}^s \in \mathcal{A}$ denotes the effective material tensor of a sample. Additionally, the class of material tensors $\mathcal{A} \in \{\mathbb{M}, \mathbb{M}_0\}$ depends on the considered problem, we follow Gajek et al. [54] and choose the constants $p, q \in \mathbb{N}_{\geq 0}$ as $p = 1$ and $q = 10$, and the operator $\|\cdot\|_1$ refers to the ℓ^1 -norm of the components in Mandel notation. The second summand in equation (3.23) encodes the simplex constraint on the weights of the DMN

$$\sum_{i=1}^{N_w} w_{K+1}^i = 1, \quad \text{where } w_{K+1}^i \geq 0, \quad (3.24)$$

in the form of a quadratic penalty term with the penalty parameter $\lambda > 0$. We implement the offline training in the Python programming language and use the machine learning framework PyTorch [76] to identify the vectors $\underline{\alpha}$ and \underline{w} . To do so, we leverage the automatic differentiation capabilities of PyTorch to solve the minimization problem

$$\mathcal{L}(\underline{\alpha}, \underline{w}) \rightarrow \min_{\underline{\alpha}, \underline{w}}, \quad (3.25)$$

using the RAdam [77] optimizer. We use mini batches of N_b samples to compute the parameter updates

$$\underline{\alpha}_{q+1} = \underline{\alpha}_q - \kappa_{q,\alpha} \frac{\partial \mathcal{L}}{\partial \underline{\alpha}}(\underline{\alpha}, \underline{w}), \quad \underline{w}_{q+1} = \underline{w}_q - \kappa_{q,w} \frac{\partial \mathcal{L}}{\partial \underline{w}}(\underline{\alpha}, \underline{w}) \quad (3.26)$$

for every epoch q . Also, we follow previous work [52–54] and use perfect binary trees without tree compression [46, 52, 53]

3.5 Online evaluation

In section 2.1, we showed that the velocity fields in layered emulsions are phase-wise affine, and thus the online evaluation procedure of direct DMNs can be employed for FDMNs as well if the phases

are kinematically unconstrained. However, for FDMNs with incompressible phases, the online evaluation procedure needs to be adapted, as we discuss in the following. We define the linear operator $\underline{\underline{A}} : (\mathbb{R}^3)^{\otimes N_n} \rightarrow (\text{Sym}_0(3))^{N_w}$ which maps the emulsion-wise jumps $\underline{\underline{b}} \in (\mathbb{R}^3)^{\otimes N_n}$ of the velocity gradient onto the phase-wise strain rate fluctuations. Also, we express the effective dissipation potential density $\bar{\Psi} : (\text{Sym}_0(3))^{N_w} \rightarrow \mathbb{R}$ of the FDMN in terms of the phase-wise dissipation potentials $\Psi_i : \text{Sym}_0(3) \rightarrow \mathbb{R}$, the respective weights w_{K+1}^i , and the phase-wise strain rate tensor $\mathbf{D}_i \in \text{Sym}_0(3)$ as

$$\bar{\Psi}(\underline{\underline{D}} + \underline{\underline{A}}\underline{\underline{b}}) = \sum_{i=1}^{N_w} w_{K+1}^i \Psi_i(\mathbf{D}_i), \quad (3.27)$$

where all entries of the vector $\underline{\underline{D}} \in (\text{Sym}_0(3))^{N_w}$ equal the effective strain rate $\bar{\mathbf{D}}$, i.e.,

$$\underline{\underline{D}} = (\bar{\mathbf{D}}, \bar{\mathbf{D}}, \dots, \bar{\mathbf{D}}). \quad (3.28)$$

Thus, the minimization problem for the online, non-linear evaluation of the FDMN is

$$\bar{\Psi}(\underline{\underline{D}} + \underline{\underline{A}}\underline{\underline{b}}) \rightarrow \min_{\underline{\underline{b}} \in (\mathbb{R}^3)^{\otimes N_n}}, \quad (3.29)$$

and the Euler–Lagrange equation of the problem (3.29) reads

$$\frac{\partial \bar{\Psi}}{\partial \underline{\underline{b}}}(\underline{\underline{D}} + \underline{\underline{A}}\underline{\underline{b}}) = \underline{\underline{A}}^\top \frac{\partial \bar{\Psi}}{\partial \underline{\underline{D}}}(\underline{\underline{D}} + \underline{\underline{A}}\underline{\underline{b}}) = 0. \quad (3.30)$$

In terms of a weight matrix $\underline{\underline{W}} : (\text{Sym}_0(3))^{N_w} \rightarrow (\text{Sym}_0(3))^{N_w}$ defined by its action on a vector $\underline{\underline{d}} \in (\text{Sym}_0(3))^{N_w}$

$$\underline{\underline{W}}\underline{\underline{d}} = \left(w_{K+1}^1 d_1, w_{K+1}^2 d_2, \dots, w_{K+1}^{N_w} d_{N_w} \right), \quad (3.31)$$

we may write the Euler–Lagrange equation (3.30) as

$$\underline{\underline{A}}^\top \underline{\underline{W}} \underline{\underline{\tau}}(\underline{\underline{D}} + \underline{\underline{A}}\underline{\underline{b}}) = 0, \quad (3.32)$$

with the vector of phase wise stresses $\underline{\underline{\tau}}(\underline{\underline{D}} + \underline{\underline{A}}\underline{\underline{b}}) \in (\text{Sym}_0(3))^{N_w}$. Therefore, the jump vector $\underline{\underline{b}}$ satisfying equation (3.32) is determined using a Newton scheme with the update rule

$$\underline{\underline{b}}_{n+1} = \underline{\underline{b}}_n + s_n \Delta \underline{\underline{b}}_n, \quad (3.33)$$

containing the iteration count n , the backtracking factor s_n , and the update direction $\Delta \underline{\underline{b}}_n$. The update direction $\Delta \underline{\underline{b}}_n$ solves the linear system

$$\underline{\underline{H}} \Delta \underline{\underline{b}}_n = \left(\underline{\underline{A}}^\top \underline{\underline{W}} \underline{\underline{\tau}}(\underline{\underline{D}} + \underline{\underline{A}}\underline{\underline{b}}) \underline{\underline{A}} \right) \Delta \underline{\underline{b}}_n = \underline{\underline{A}}^\top \underline{\underline{W}} \underline{\underline{\tau}}(\underline{\underline{D}} + \underline{\underline{A}}\underline{\underline{b}}). \quad (3.34)$$

So far, the procedure is completely analogous to the approaches for (direct) DMNs presented in previous work [46, 54, 59]. However, in the case of incompressible phases, the matrix $\underline{\underline{A}}$ is symmetric but singular, and the solution of the equation system (3.34) is not unique. However, because of incompressibility, we know that the i -th entry \mathbf{b}_i of the jump vector $\underline{\underline{b}}$ is orthogonal to the i -th entry \mathbf{n}_i of the vector of layering normals $\underline{\underline{n}}$, i.e.,

$$\mathbf{b}_i \cdot \mathbf{n}_i = 0. \quad (3.35)$$

Hence, we construct the block diagonal matrix $\underline{\underline{N}} : (\mathbb{R}^3)^{\otimes N_n} \rightarrow (\mathbb{R}^3)^{\otimes N_n}$ consisting of N_w blocks \mathbf{N}_i on the main diagonal, which are defined as

$$\mathbf{N}_i = \beta_i \mathbf{n}_i \otimes \mathbf{n}_i, \quad i \in \{1, \dots, N_w\} \quad (3.36)$$

with the constant $\beta_i \in \mathbb{R}_{>0}$. By definition it holds that

$$\mathbf{N}_i \mathbf{b}_i = \mathbf{0}, \quad (3.37)$$

and the jump vector \underline{b} is in the kernel of \underline{N} , such that

$$\underline{N} \underline{b} = \underline{0}. \quad (3.38)$$

Thus, we add equations (3.34) and (3.38), such that the solution $\Delta \underline{b}_n$ of the resulting update rule

$$(\underline{H} + \underline{N}) \Delta \underline{b}_n = \underline{A}^\top \underline{W}_\tau (\underline{D} + \underline{A} \underline{b}), \quad (3.39)$$

is unique. However, floating point precision may cause issues during the addition of the operators \underline{H} and \underline{N} , if numbers of largely different magnitudes are summed. To remedy this issue, the scalars β_i need to be chosen according to the magnitude of the entries in the matrix \underline{H} . Furthermore, some input weights w_{K+1}^i might become equal to, or close to zero during training, which might render the system matrix $(\underline{H} + \underline{N})$ ill-conditioned. Thus, it might be difficult to obtain accurate update directions $\Delta \underline{b}_n$ by solving equation (3.39). While it is generally possible to prune the FDMN tree [53] by removing phases with vanishing or almost vanishing volume fractions, this might collapse the rank-3 CLMs of the bottom FDMN layer into layered materials of a lesser rank. In case of infinite material contrast, this could result in the propagation of singular effective properties through the FDMN. It is therefore preferable to work with possibly ill-conditioned systems and to employ appropriate methods for the solution of ill-conditioned systems [78]. Alternatively, multiple FDMNs can be trained and the ones with the best online evaluation results can be selected. In this article, we follow the latter approach.

4 Application to rigid fibers suspended in polyamide 6

4.1 Material description and computational aspects

Let a fiber orientation state be defined by the fiber orientation distribution function $\rho : \mathcal{S}^2 \rightarrow \mathbb{R}$, which encodes the probability that fibers are oriented in the direction $\mathbf{p} \in \mathcal{S}^2$. In component scale molding simulations, the orientation distribution function ρ is often spatially inhomogeneous, and it is therefore prohibitively expensive to compute the spatial and temporal evolution of the function ρ [79,80]. Therefore, the evolution of surrogate quantities that contain some of the information encoded in the function ρ is often considered instead. One such quantity is the second order fiber orientation tensor [81,82]

$$\mathbf{N} = \int_{\mathcal{S}^2} \mathbf{p} \otimes \mathbf{p} \rho(\mathbf{n}) dS(\mathbf{n}), \quad (4.1)$$

which is commonly used in component scale molding simulations to track the evolution of the fiber orientation state [79,80]. Because a major prospect of FDMNs is the combination of component scale molding simulations with high fidelity information from full field viscous computations, we employ the orientation tensor \mathbf{N} to describe the fiber orientation state of the considered microstructures. The tensor \mathbf{N} may be parametrized by its two largest eigenvalues λ_1 and λ_2 , as well as a proper orthogonal tensor \mathbf{R} via [83,84]

$$\mathbf{N} = \mathbf{R} \mathbf{diag}(\lambda_1, \lambda_2, 1 - \lambda_1 - \lambda_2) \mathbf{R}^\top, \quad \lambda_1 \geq \lambda_2. \quad (4.2)$$

By objectivity [51], and because the tensor \mathbf{N} has unit trace and is positive semi-definite, every fiber orientation tensor \mathbf{N} represents a point in the fiber orientation triangle S_\top [55,84]

$$S_\top = \left\{ \underline{\lambda} = (\lambda_1, \lambda_2)^\top \mid 1 \geq \lambda_1 \geq \frac{1}{3} \quad \text{and} \quad \min(\lambda_1, 1 - \lambda_1) \geq \lambda_2 \geq \frac{1 - \lambda_1}{2} \right\}. \quad (4.3)$$

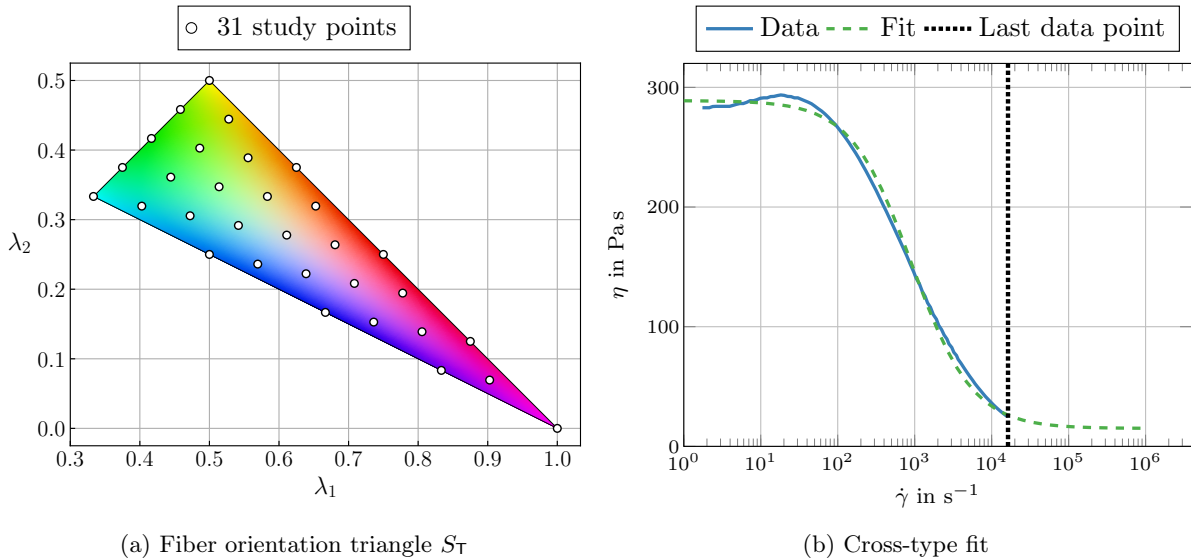


Figure 5: Fiber orientation triangle S_T in CMYK coloring with 31 evaluation points (a), and material data with Cross-type fit for Ultramid®B3K (b).

For detailed discussions regarding the description of fiber orientation states, we refer the reader to Kanatani [81] and Bauer et al. [84, 85]. To generate the training data and the online validation data for the FDMN, we use FFT-based computational procedures to compute the effective viscous response of fiber suspensions [17, 38]. We generate the required fiber suspension microstructures using the sequential addition and migration method [86] for 31 orientation states $\underline{\lambda}$ in the fiber orientation triangle S_T , see Figure 7. For the visualization of the orientation triangle S_T , we follow Köbler et al. [55], and use a CMYK coloring scheme. To keep the computational effort for computing the effective viscous responses feasible, we restrict to microstructures with a fiber volume fraction of 25%, and assign all fibers the length ℓ and the diameter d . Also, we set the aspect ratio $r_a = \ell/d$ of all fibers to 10, and use the results of Sterr et al. [17] regarding the required resolution and size of the microstructure volume elements. Consequently, we choose a resolution of 15 voxels per fiber diameter, as well as cubic volume elements with edge size $L = 2.2\ell$. Regarding the matrix material, we build on the investigations in Sterr et al. [17, 51], and prescribe a commercially available polyamide 6 [87] as the matrix material. We fit a Cross-type constitutive equation

$$\eta(\dot{\gamma}) = \eta_\infty + \frac{\eta_0 - \eta_\infty}{1 + (k\dot{\gamma})^m}, \quad (4.4)$$

to the available material data in the interval $[1.7, 16300] \text{ s}^{-1}$ at a temperature of 250°C , and collect the resulting model parameters in Table 1. For all non-Newtonian considerations, we investigate the six load

η_0	η_∞	k	m
288.9 Pa s	15.0 Pa s	$10.9 \cdot 10^{-4} \text{ s}$	1.1

Table 1: Parameters of the Cross-type constitutive equation (4.4) for a commercially available polyamide 6 [87].

cases collected in the matrix $\underline{\underline{D}}$ in Mandel notation

$$\underline{\underline{D}} = \dot{\gamma} \sqrt{\frac{2}{3}} \begin{bmatrix} 1 & -\frac{1}{2} & -\frac{1}{2} & 0 & 0 & 0 \\ -\frac{1}{2} & 1 & -\frac{1}{2} & 0 & 0 & 0 \\ -\frac{1}{2} & -\frac{1}{2} & 1 & 0 & 0 & 0 \\ 0 & 0 & 0 & \sqrt{\frac{3}{2}} & 0 & 0 \\ 0 & 0 & 0 & 0 & \sqrt{\frac{3}{2}} & 0 \\ 0 & 0 & 0 & 0 & 0 & \sqrt{\frac{3}{2}} \end{bmatrix}, \quad (4.5)$$

or each macroscopic scalar shear rate $\dot{\gamma}$ in the set of studied shear rates $S_{\dot{\gamma}}$, such that

$$\dot{\gamma} \in S_{\dot{\gamma}} = \{a \cdot 10^b \text{ s}^{-1} \mid a = 1, 2, 5; b = 1, 2, 3, 4\} \cup \{10^5 \text{ s}^{-1}\}. \quad (4.6)$$

Consequently, the set $\bar{\mathbf{D}}_{\dot{\gamma}}$ of all investigated load cases is defined by the equations (4.5) and (4.6). Because the viscous stress inside the rigid fibers is, constitutively, not well-defined [17], we employ a dual formulation of the associated homogenization problem for the FFT-based computations. We discretize the microstructures on a staggered grid [88], and solve the resulting equation systems with the conjugate gradient method (CG) for linear computations, and with a Newton-CG approach for non-linear computations. With the goal of training an FDMN for each of the 31 fiber orientation states shown in Figure 5(a), we generate 32 sample viscosities with the procedure described in section 3.3, and compute the corresponding effective viscosities. To compute a single effective viscosity, five FFT-based computations are necessary [38], leading to a total of 4960 computations, and 992 computed effective viscosities. In the previous sections 2.3 and 3.2, we studied the linear homogenization functions of CLMs, and presented the FDMN architecture to treat infinite material contrast and incompressible materials. In the following, we discuss the material sampling for the offline training, the offline training procedure, and the online evaluation of FDMNs for suspensions of rigid particles.

4.2 Offline training

With the linear training data at hand, we wish to train FDMNs for the prediction of the non-Newtonian viscous behavior of shear-thinning fiber polymer suspensions. We follow previous work [46, 54] and choose the depth of the FDMN as $K = 8$ to achieve sufficient prediction quality for non-linear computations. An FDMN of depth $K = 8$ with CLMs of rank $R = 3$ has 512 weights and 638 angles as free parameters, as per equations (3.6) and (3.20). For each microstructure, we define the training data \mathcal{S}^D as

$$\mathcal{S}^D = \{(\mathbb{V}_1^s, \mathbb{V}_F, \bar{\mathbb{V}}^s) \mid s \in (1, \dots, 32)\}, \quad (4.7)$$

where \mathbb{V}_1^s denotes the sample viscosities generated with equation (3.7), \mathbb{V}_F denotes the infinite viscosity of the rigid fibers, and $\bar{\mathbb{V}}^s$ stands for the effective viscosity of the sample s . For each microstructure, we split the training data \mathcal{S}^D into the training set $\mathcal{S}^t \subset \mathcal{S}^D$ and the validation set $\mathcal{S}^v \subset \mathcal{S}^D$, which consist of 90% and 10% of the total training data, respectively. The training set \mathcal{S}^t and the validation set \mathcal{S}^v share no samples, i.e., $\mathcal{S}^t \cap \mathcal{S}^v = \emptyset$.

As an initial guess for the FDMN parameters, we uniformly sample all angles $\underline{\alpha}$ and weights \underline{w} from their respective intervals, and rescale the weights \underline{w} such that they sum to unity. Because we use a relatively small set of 32 samples as training data, we dedicate a large portion of it to the training set \mathcal{S}^t , and choose to train 20 FDMNs per fiber orientation state $\underline{\lambda}$. Furthermore, we train the FDMNs on mini batches with size $N_b = 8$, for which we draw randomly from the training set \mathcal{S}^t . In case the last batch is smaller than eight samples, we drop the batch. Because the initialization of the parameter vectors $\underline{\alpha}$ and \underline{w} , as well

as the offline training process are random, the FDMNs differ in their parameters and quality of fit. By training 20 FDMNs per fiber orientation state, we leverage this randomness with the goal of obtaining FDMNs with a high quality of fit. This strategy aims to reduce the total computational effort required to obtain sufficiently accurate FDMNs, because repeatedly training FDMNs on 32 samples requires less computational resources than conducting full field simulations for larger sample sizes. For the minimization of the loss function \mathcal{L} , we choose the RAdam algorithm [77] and use a learning rate sweep [89] to determine the learning rates $\kappa_{0,\alpha}$ and $\kappa_{0,w}$. With the learning rate sweep we obtain highly similar learning rates for both parameter groups $\underline{\alpha}$ and \underline{w} , such that $\kappa_{0,\alpha} = \kappa_{0,w} = 1 \cdot 10^{-2}$. As the learning process advances, we use PyTorch’s StepLR learning rate scheduler to improve convergence towards minima [90,91]. To do so, we multiply the learning rates $\kappa_{0,\alpha}$ and $\kappa_{0,w}$ with a constant factor $f_{LR} = 0.75$ every 150 epochs. Other than the learning rates, we used standard hyperparameters for the two momentum coefficients $\beta_1 = 0.9$ and $\beta = 0.999$, as well as the stabilization constant $\varepsilon = 10^{-8}$. Overall, we train every FDMNs for a total of 2000 epochs each.

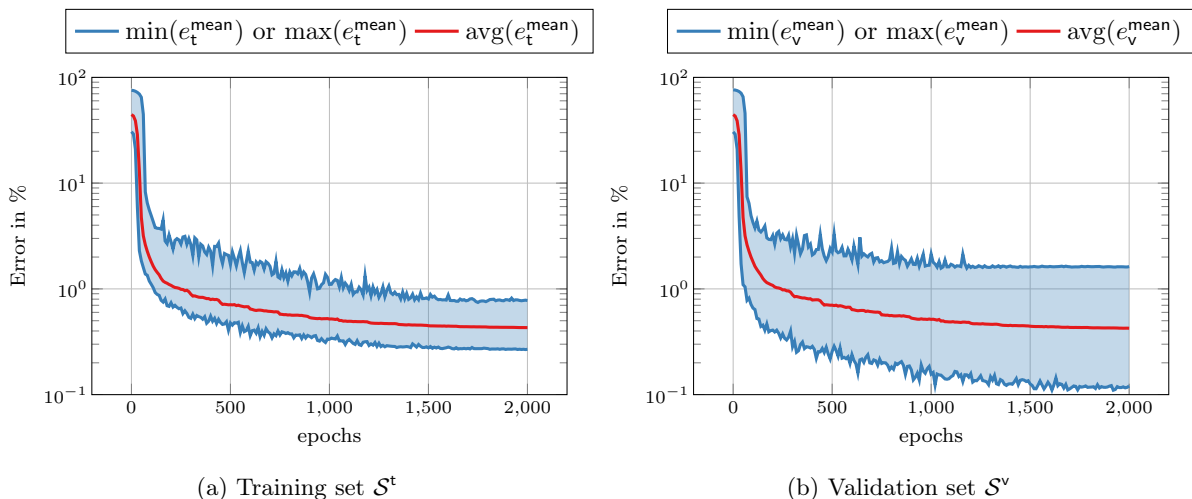


Figure 6: Minimum, maximum, and average mean error e^{mean} of all trained FDMNs for the training set \mathcal{S}^t (a) and the validation set \mathcal{S}^v (b).

To measure the quality of fit, we define the mean error e^{mean} over a subset \mathcal{S} of the training data \mathcal{S}^D as

$$e^{\text{mean}} = \frac{1}{|\mathcal{S}|} \sum_{(\mathbb{V}_1^s, \mathbb{V}_F, \mathbb{V}^s) \in \mathcal{S}} \frac{\|\mathcal{DMN}_L(\mathbb{V}_1^s, \mathbb{V}_F, \underline{\alpha}, \underline{w}) - \mathbb{V}^s\|_1}{\|\mathbb{V}^s\|_1}, \quad (4.8)$$

where $|\mathcal{S}|$ is the cardinality of the set \mathcal{S} . Depending on the fiber orientation state $\underline{\lambda}$ and the initial guesses of the angles $\underline{\alpha}$ and the weights \underline{w} , the quality of fit varies per DMN. Therefore, for the whole training process of all 620 FDMNs, we visualize the smallest mean error $\min(e^{\text{mean}})$, the largest mean error $\max(e^{\text{mean}})$, and the average mean error $\text{avg}(e^{\text{mean}})$ for the training and validation sets \mathcal{S}^t and \mathcal{S}^v per epoch in Figure 6. For the training and the validation set, we observe that the three considered error measures drop rapidly at the beginning of the training, and continue to improve as the training continues. As the learning rates are small for epochs larger than 1500, the errors do not change significantly at the end of the training, and convergence is ensured. Evidently, the largest mean error $\max(e_t^{\text{mean}})$ on the training set \mathcal{S}^t drops below 1% at the end of the training process, while the smallest mean error $\min(e_t^{\text{mean}})$ falls below 0.3%. This indicates a high quality of fit on the training set \mathcal{S}^t for all FDMNs. Compared to the training set \mathcal{S}^t , the spread between the largest mean error $\max(e_v^{\text{mean}})$ and the smallest mean error $\min(e_v^{\text{mean}})$ for the validation set \mathcal{S}^v is larger. However, the largest mean error $\max(e_v^{\text{mean}})$ stays

below 2% for all considered FDMNs and does not fluctuate by a large margin. Additionally, the average mean error $\text{avg}(e_v^{\text{mean}})$ decreases continuously during training. Consequently, the prediction quality on both the training and validation set improve on average as the training progresses, although the largest mean validation error $\max(e_v^{\text{mean}})$ does not improve significantly after 1250 training epochs. Overall, this indicates that no pronounced overfitting to the training data set \mathcal{S}^t occurs.

4.3 Online evaluation

To measure the online performance of an FDMN, we define the online error function $e_{\text{on}} : \text{Sym}_0(3) \rightarrow \mathbb{R}$ as

$$e_{\text{on}}(\bar{\mathbf{D}}) = \frac{\|\boldsymbol{\sigma}^{DMN}(\bar{\mathbf{D}}) - \boldsymbol{\sigma}^{FFT}(\bar{\mathbf{D}})\|_2}{\|\boldsymbol{\sigma}^{FFT}(\bar{\mathbf{D}})\|_2}, \quad (4.9)$$

where $\|\cdot\|_2$ denotes the ℓ^2 -norm of the components in Mandel notation, $\bar{\mathbf{D}}$ stands for the prescribed effective strain rate tensor, and $\boldsymbol{\sigma}^{DMN} : \text{Sym}_0(3) \rightarrow \text{Sym}_0(3)$ and $\boldsymbol{\sigma}^{FFT} : \text{Sym}_0(3) \rightarrow \text{Sym}_0(3)$ are the stress functions of the FDMN and the FFT-based homogenization, respectively. We then choose the largest error over all load cases $e_{\text{on}}^{\text{max}}$ and the mean error over all load cases $e_{\text{on}}^{\text{mean}}$

$$e_{\text{on}}^{\text{max}} = \max_{\bar{\mathbf{D}} \in \bar{\mathcal{D}}_{\dot{\gamma}}} e_{\text{on}}, \quad e_{\text{on}}^{\text{mean}} = \frac{1}{|\bar{\mathcal{D}}_{\dot{\gamma}}|} \sum_{\bar{\mathbf{D}} \in \bar{\mathcal{D}}_{\dot{\gamma}}} e_{\text{on}}(\bar{\mathbf{D}}), \quad (4.10)$$

to study the performance of the different FDMNs. For each investigated orientation state $\underline{\lambda}$, we identify the FDMN with the smallest maximum error $e_{\text{on}}^{\text{max}}$ and visualize the associated errors $e_{\text{on}}^{\text{mean}}$ and $e_{\text{on}}^{\text{max}}$ over the fiber orientation triangle, see Figures 7(a) and 7(b)

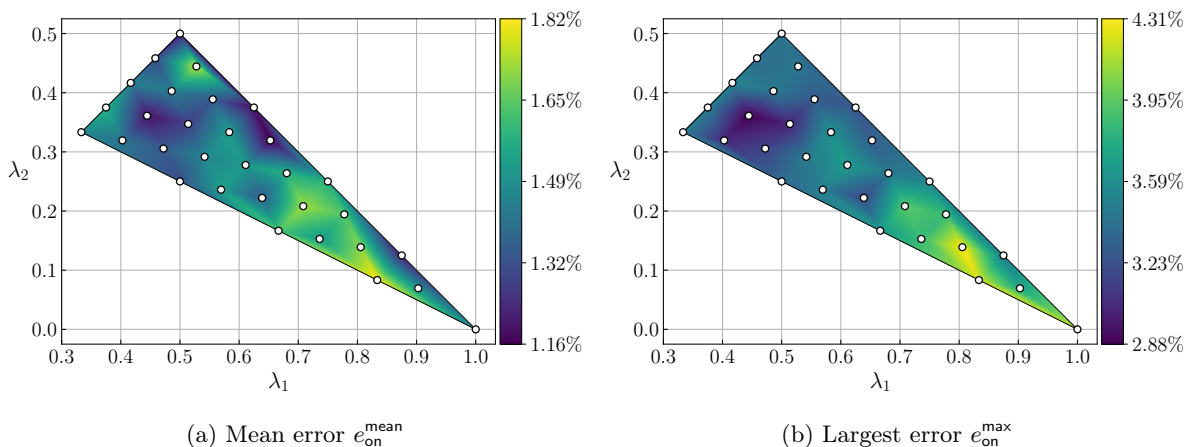


Figure 7: Mean online error $e_{\text{on}}^{\text{mean}}$ (a) and largest online error $e_{\text{on}}^{\text{max}}$ (b) for the best FDMNs over the fiber orientation triangle.

The maximum error $e_{\text{on}}^{\text{max}}$ of the best FDMNs range between 2.88% for the orientation state $\underline{\lambda} = (0.4444, 0.3611)^\top$, and 4.31% for the fiber orientation state $\underline{\lambda} = (0.8055, 0.1389)^\top$. Thus, for the investigated orientation states, the FDMNs yield sufficient prediction accuracy in terms of engineering requirements over a wide range of shear rates $\dot{\gamma} \in [10, 10^5] \text{ s}^{-1}$. Additionally, the relatively low maximum errors $e_{\text{on}}^{\text{max}}$ show that with fewer samples than in previous studies for solid materials, for example by Liu et al. [52, 53] or Gajek et al. [46, 54, 59], appropriately accurate FDMNs can be produced for suspensions of rigid fibers. Generally, the maximum error $e_{\text{on}}^{\text{max}}$ is larger for more strongly aligned oriented orientation states towards the lower right-hand side of the fiber orientation triangle than for less strongly

aligned oriented orientation states towards the upper and the left-hand side. The mean error $e_{\text{on}}^{\text{mean}}$ ranges between 1.16% for the orientation state $\underline{\lambda} = (0.8334, 0.0833)^\top$, and 1.82% for the orientation state $\underline{\lambda} = (0.6528, 0.3194)^\top$, underlining the prediction accuracy of the FDMNs.

To discuss one specific example, we take a more detailed look at the performance of the best FDMN at the fiber orientation state $\underline{\lambda} = (0.8055, 0.1389)^\top$ where the largest maximum error $e_{\text{on}}^{\text{max}} = 4.31\%$ occurs. Let the components of the strain rate tensor $\tilde{\mathbf{D}}_i \in \text{Sym}_0(3)$, in the standard basis $\{\mathbf{e}_i\}$ and in Mandel notation, be given by the i -th column of the matrix $\underline{\underline{\mathbf{D}}}/\dot{\gamma}$, see equation (4.5). Then, the tensor $\tilde{\mathbf{D}}_i$ represents a load with unit norm, and we refer to the tensor $\tilde{\mathbf{D}}_i$ as load case. In the following, we discuss the observed stress responses and the prediction quality of the FDMN for all considered shear rates (4.6) and the six load cases defined in equation (4.5), see Figure 8. Because of the strong alignment of the fibers in the coordinate direction \mathbf{e}_1 , the stress norms are the largest for the load case $\tilde{\mathbf{D}}_1$, which encodes incompressible elongational flow in the coordinate direction \mathbf{e}_1 , see Figure 8(a).

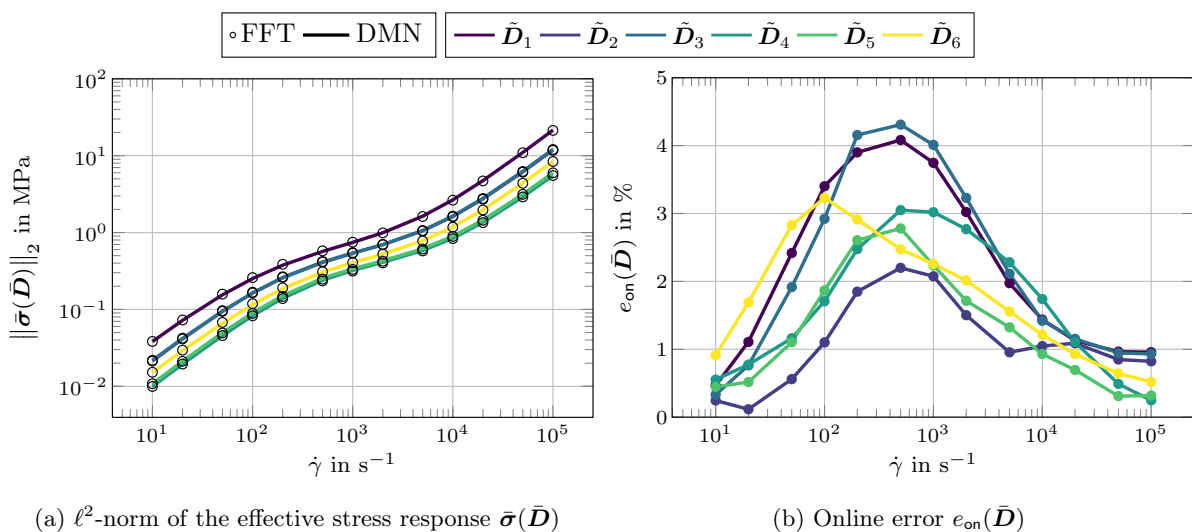


Figure 8: ℓ^2 -norm of the effective stress response $\bar{\sigma}(\tilde{\mathbf{D}})$ over the shear rate $\dot{\gamma} \in [10, 10^5] \text{ s}^{-1}$ at the orientation state $\underline{\lambda} = (0.8055, 0.1389)$ as computed with FFT-based homogenization and the best identified FDMN (a). Online error $e_{\text{on}}(\tilde{\mathbf{D}})$ of the FDMN over the shear rate $\dot{\gamma} \in [10, 10^5] \text{ s}^{-1}$ (b).

The norms of the stress responses to elongational flow in the coordinate directions \mathbf{e}_2 and \mathbf{e}_3 , i.e., the load cases $\tilde{\mathbf{D}}_2$ and $\tilde{\mathbf{D}}_3$, are comparatively small. For the largest considered shear rate of $\dot{\gamma} = 10^5 \text{ s}^{-1}$, we observe a stress norm of 21 MPa for the load case $\tilde{\mathbf{D}}_1$, as well as 11.8 MPa and 12.1 MPa for the load cases $\tilde{\mathbf{D}}_2$ and $\tilde{\mathbf{D}}_3$, respectively. Because of the similar degrees of fiber alignment in the coordinate directions \mathbf{e}_2 and \mathbf{e}_3 , the stress norms associated with the load cases $\tilde{\mathbf{D}}_2$ and $\tilde{\mathbf{D}}_3$ differ only slightly. Furthermore, the stress norms in response to shear in the load cases $\tilde{\mathbf{D}}_4$ and $\tilde{\mathbf{D}}_5$ are smaller than to shear in the load cases $\tilde{\mathbf{D}}_6$. Again, this is caused by the strong alignment of the fibers in the coordinate direction \mathbf{e}_1 , which increases the flow resistance stronger in the \mathbf{e}_1 - \mathbf{e}_2 -plane than in other shear planes [51]. For the largest considered shear rate of $\dot{\gamma} = 10^5 \text{ s}^{-1}$, the stress norms are 5.5 MPa, 6.0 MPa, and 8.4 MPa for the load cases $\tilde{\mathbf{D}}_4$, $\tilde{\mathbf{D}}_5$, and $\tilde{\mathbf{D}}_6$, respectively. Overall, the predicted ℓ^2 -norm of the effective stress response $\bar{\sigma}^{\text{DMN}}$ of the FDMN agrees closely with the effective stress $\bar{\sigma}^{\text{FFT}}$ computed via FFT-based homogenization for all investigated load directions $\tilde{\mathbf{D}}_i$, $i \in \{1, \dots, 6\}$, and shear rates $\dot{\gamma} \in S_{\dot{\gamma}}$, see Figure 8(a).

Not only the ℓ^2 -norm of the effective stress response is predicted well by the FDMN, but the direction as well. This is evident from the relatively small online errors $e_{\text{on}}(\tilde{\mathbf{D}})$ shown in 8(b). Depending on the load case, the error e_{on} increases up to a point in the interval $[10^2, 10^3] \text{ s}^{-1}$, before decreasing again for

higher shear rates. The largest error occurs for the elongational load case $\tilde{\mathbf{D}}_3$ with 4.31%, and is closely followed by 4.08% for the elongational load case $\tilde{\mathbf{D}}_1$. For the shear load cases $\tilde{\mathbf{D}}_4$, $\tilde{\mathbf{D}}_5$, and $\tilde{\mathbf{D}}_6$, the largest errors are 3.05%, 2.78%, and 3.23%, respectively, while the largest error for the elongational load case $\tilde{\mathbf{D}}_2$ is 2.2%. The largest error for the shear load case $\tilde{\mathbf{D}}_6$ occurs at a shear rate of $\dot{\gamma} = 10^2 \text{ s}^{-1}$, whereas the largest errors for all other load cases occur at a shear rate of $\dot{\gamma} = 5 \cdot 10^2 \text{ s}^{-1}$. This is directly tied to the Cross-type constitutive equation (4.4), which has two Newtonian plateaus for low and high shear rates and a non-linear transition in between. Consequently, for large shear rates $\dot{\gamma} \rightarrow \infty$ the Matrix behavior is Newtonian and the homogenization function of the microstructure approaches the linear homogenization function. Since the FDMN approximates the non-linear homogenization function the microstructure to first order [54], the prediction quality depends on the degree to which the matrix behaves non-linearly. This is in line with previous observations regarding the modelling of shear-thinning fiber suspensions [17, 51].

4.4 Computational Speedup

	Sampling total	Sampling per orientation (mean)	Training
CPU Hours	24415	788	0.08
Wall-clock time (h)	305	9.8	0.08

Table 2: CPU hours and wall-clock time for the training of one FDMN and the sampling of effective viscosities \bar{V}^s using FFT-based homogenization.

	FFT (h)	DMN (ms)	Speedup
Min	2.08	600	11785
Mean	2.61	630	14828
Max	3.07	650	17225

Table 3: Speedups and wall-clock times for the evaluation of a single load case using FFT-based homogenization compared to an FDMN.

For sampling the linear homogenization functions of the 31 considered fiber orientation states $\underline{\lambda} \in S_T$, we used a workstation with two AMD EPYC 7552 48-Core processors and 1024 GB DRAM. We relied on a single thread per FFT-based computation and ran 80 computations in parallel. In total, the computations took 24415 CPU hours and a wall-clock time of 305 hours, see Table 2. Averaging over all 31 considered orientations $\underline{\lambda}$, this leads to 788 CPU Hours and 9.8h wall-clock time per orientation. For the training and the online evaluation of the FDMNs, as well as the non-linear FFT-based computations, we used a workstation with two AMD EPYC 9534 64-Core Processors and 1024 GB DRAM, and ran all computations on a single thread. The wall-clock time to evaluate all six load cases $\tilde{\mathbf{D}}_i$, $i = 1, \dots, 6$, and thirteen shear rates $\dot{\gamma} \in S_{\dot{\gamma}}$ in series for a single fiber orientation state $\underline{\lambda}$ is listed in Table 3. The wall-clock times for the FFT-based computations range from 2.08h to 3.07h with the mean wall-clock time over all considered orientation states $\underline{\lambda}$ being 2.61h. In contrast, the online evaluation of the FDMNs takes between 600ms and 630ms, with a mean of 650ms. Consequently, the speedup factors range between 11785 and 17225 with a mean of 14828. This considerable speedup is achieved by investing computational resources into the sampling of the linear homogenization functions of the microstructures. It is straightforward to judge whether this investment is sensible for the considered setup. For one microstructure the

generation of training data and the training of a single FDMN takes 9.88h wall-clock time on average, while the non-linear FFT-based computations take 2.61h wall-clock time on average. Therefore, assuming the non-linear computations run on one thread as in the presented setup, it would take four non-linear computation to offset the initial investment into an FDMN on average. Given that component scale simulations routinely require thousands or millions of microscale computations [46, 59], the sampling and training effort is offset easily in engineering problems.

4.5 Comparison with machine learning aided analytical models

In this section, we compare the FDMN based approach to predicting the effective behavior of fiber suspensions with another machine learning approach suggested by Sterr et al. [51]. The authors presented four different analytical constitutive equations for the effective viscosity of shear-thinning fiber suspensions, and identified the model parameters using supervised machine learning. The model parameters were learned from simulation data obtained with FFT-based computational techniques for the same material as considered in this article: rigid fibers suspended in a Cross-type matrix material with parameters as shown in Table 1. However, the FDMN approach and the analytical approach follow very different paradigms. The FDMNs are trained to approximate the non-linear homogenization function of the microstructure by learning the respective *linear* homogenization function without prior knowledge of the actual constitutive equations. In contrast, the parameters of the analytical models were learned from the *non-linear* stress response of the suspension, and the analytical models incorporate knowledge about the expected material behavior. Even though the two approaches follow different strategies, they achieve comparable prediction accuracy. For the load cases $\bar{\mathbf{D}}_\gamma$ and fiber orientation states $\underline{\lambda}$ considered in this article, the largest validation error of the FDMNs is 4.31% and occurs for the fiber orientation state $\underline{\lambda} = (0.8055, 0.1389)^\top$. For the same load cases $\bar{\mathbf{D}}_\gamma$ and the same set of fiber orientation states $\underline{\lambda}$, three of the four analytical models by Sterr et al. [51] achieve a maximum prediction error of 5.00%, which occurs for the fiber orientation state $\underline{\lambda} = (0.8334, 0.0833)^\top$. The fourth model did not compare favorably with the other three, because the built-in assumptions of stress-strain rate superposition and orientation averaging did not hold well for the considered suspension [51]. Consequently, the FDMNs achieved a slightly higher prediction accuracy for the type of fiber suspension considered in this article. Also, within the constraints of a first order approximation, FDMNs generalize to different constitutive equations while the presented analytical models do not, reducing the required modelling effort for FDMNs. However, the FDMNs utilized in this article use 1150 free parameters, whereas the analytical models use between 11 and 49 parameters.

In terms of computational cost, generating the training data and training an FDMN for a single microstructure took 9.88h wall-clock time on average, see Table 2. The parameters of the analytical models for a single microstructure were identified based on six non-linear FFT-based simulations, which took 2.61h wall-clock time on average. This leads to an average total wall-clock time of 15.70h if all required simulations are run in series on one thread, and 0.04h are allocated to identify the model parameters. However, with the considered setup, the non-linear FFT-based simulations could be run in parallel, such that the analytical model parameters can be obtained more quickly than an FDMN. In summary, FDMNs offer a higher degree of accuracy and flexibility regarding the considered constitutive equations, but require more computational resources and a larger amount of parameters. Furthermore, FDMNs are inherently thermodynamically consistent [54, §3.1], and inherit stress-strain rate monotonicity from their phases [54, App. C]. In contrast, both thermodynamic consistency and stress-strain rate monotonicity must be ensured manually in constitutive models.

5 Conclusions

In this article, we extended the direct DMN architecture to the Flexible DMN (FDMN) architecture for the treatment of fiber suspensions with infinite material contrast and shear-thinning matrix behavior. To do so, we derived linear homogenization functions for two-phase layered emulsions that are governed by Stokes flow and consist of linearly viscous phases. More specifically, we utilized results by Kabel et al. [70] and Milton [69] on the homogenization of laminates to derive closed form analytical expressions for the effective properties of such layered emulsions. Because rank-one layered materials are ill-suited as DMN building blocks in case of infinite material contrast, we investigated the effective properties of coated layered materials (CLMs). We leveraged the linear homogenization functions of rank-one layered materials and investigated under which conditions the effective behavior of CLMs is non-singular if the core material is rigid. The conditions depend on the physical constraints of the employed materials, and involve the rank of the CLM and the relative orientation of the layering directions. In the relevant case for incompressible fiber suspensions, a CLM consists of an incompressible coating material and a rigid core material. Then, the effective viscosity of a rank-3 CLM is non-singular if the three layering directions are mutually non-orthogonal and mutually non-collinear.

Using the derived homogenization functions for layered materials and CLMs, we extended the (direct) DMN architecture to the FDMN architecture by replacing the lowest layer of rank-one laminates in a (direct) DMN with non-singular CLMs, and the other rank-one laminates with rank-one layered materials capable of treating fluids. For the offline training of an FDMN, we presented a strategy where the relative angles of the CLM layering directions are fixed to reduce the amount of free parameters and guarantee non-singular CLMs. Furthermore, we modified the online evaluation strategy of direct DMNs to account for incompressible phases. We leveraged the FDMN architecture to predict the non-linear effective behavior of fiber suspensions with a Cross-type matrix material. Compared to direct numerical simulations with FFT-based computational techniques, the FDMNs achieved validation errors below 4.31% for a variety of 31 fiber orientation states, six different load cases, and a wide range of shear rates relevant to engineering processes. If the time required to generate the training data and train the FDMNs is not considered, the FDMNs achieved an average speed up factor of 14828 as compared to FFT-based simulations. Additionally, FDMNs achieve higher accuracy than another machine learning based approach by Sterr et al. [51] for the same composite material. However, this competitive accuracy improvement comes at the cost of an increased computational effort to obtain the training data for the FDMNs.

In future work, the application and extensions of the FDMN architecture to problems involving more than two phases, where multiple phases may be singular, could be explored. This could enable the FDMN based treatment of three-phase systems containing a fluid, fibers, and gas, which occur in engineering processes like injection molding [92] and flotation de-inking [93]. Furthermore, problems involving solids with defects could be explored as well. To account for the locally varying microstructure in component scale simulations, fiber orientation interpolation schemes [46, 57, 63] could be combined with the FDMN architecture to increase versatility, and enable new concurrent two-scale simulations involving defects and rigid inclusions.

Declaration of competing interest

The authors declare that they have no known competing financial interests or personal relationships that could have appeared to influence the work reported in this paper.

Data availability

The data that support the findings of this study are available from the corresponding author upon reasonable request.

Acknowledgements

The research documented in this manuscript was funded by the Deutsche Forschungsgemeinschaft (DFG, German Research Foundation), project number 255730231, within the International Research Training Group “Integrated engineering of continuous-discontinuous long fiber-reinforced polymer structures“ (GRK 2078/2). The support by the German Research Foundation (DFG) is gratefully acknowledged.

Author contributions

The present study was conceptualized by B. Sterr, M. Schneider and T. Böhlke. The presented FDMN architecture was derived by B. Sterr, S. Gajek, M. Schneider, and T. Böhlke. B. Sterr, S. Gajek, and M. Schneider implemented and validated the software. B. Sterr performed the simulations, analyzed and visualized the data, and drafted the manuscript. The original manuscript draft was extensively reviewed and edited by B. Sterr, A. Hrymak, M. Schneider, and T. Böhlke. Resources were provided by M. Schneider and T. Böhlke. The research project was supervised by A. Hrymak, M. Schneider and T. Böhlke.

Appendix

A Coated layered materials with singular core

A.1 Singularity condition for coated layered materials with singular core

In the particular cases that the core material m_1 of a CLM is rigid or represents a void, the dual or the primal material properties \mathbb{K}_1 or \mathbb{M}_1 approach zero, respectively. Thus, more generally, we let the material tensor \mathbb{A}_1 approach zero, and rewrite equation (2.42) as

$$\lim_{\mathbb{A}_1 \rightarrow \mathbf{0}} \bar{\mathbb{A}} = \mathbb{A}_2 \left(\mathbb{I} + (1 - f_2) \left(-\mathbb{I} + f_2 \sum_{r=1}^R c_r \Gamma_{\mathbb{A}_2}(\mathbf{n}_r) \mathbb{A}_2 \right)^{-1} \right). \quad (5.1)$$

In the following, we study under which conditions the effective material properties $\bar{\mathbb{A}}$ of a rank- R CLM are singular. The effective material properties $\bar{\mathbb{A}}$ are singular precisely if there exists an effective tensor $\bar{\mathbf{g}} \in \{\text{Sym}(3), \text{Sym}_0(3)\}$, such that

$$\bar{\mathbb{A}}[\bar{\mathbf{g}}] = \mathbf{0}. \quad (5.2)$$

Using the definition (5.1), equation (5.2) may be equivalently rewritten in the form

$$\left(\sum_{r=1}^R c_r \Gamma_{\mathbb{A}_2}(\mathbf{n}_r) \mathbb{A}_2 \right) [\bar{\mathbf{g}}] = \bar{\mathbf{g}}. \quad (5.3)$$

Equation (5.3) is satisfied precisely if $\bar{\mathbf{g}}$ lies in the intersection of all subspaces $\mathcal{E}_r^{\mathbb{A}}$, such that

$$\bar{\mathbf{g}} \in \bigcap_{r=1}^R \mathcal{E}_r^{\mathbb{A}}, \quad (5.4)$$

or, equivalently,

$$\Gamma_{\mathbb{I}}(\mathbf{n}_r)[\bar{\mathbf{g}}] = \bar{\mathbf{g}}, \quad \forall r \in \{1, \dots, R\}. \quad (5.5)$$

We prove this as follows. First, if $\bar{\mathbf{g}}$ lies in the section of all subspaces such that (5.4) is satisfied, it follows from equation (5.5) and the definition of the operator $\Gamma_{\mathbb{A}_2}(\mathbf{n}_r)$ (2.41) that

$$\left(\sum_{r=1}^R c_r \Gamma_{\mathbb{A}_2}(\mathbf{n}_r) \mathbb{A}_2 \right) [\bar{\mathbf{g}}] = \left(\sum_{r=1}^R c_r \Gamma_{\mathbb{A}_2}(\mathbf{n}_r) \mathbb{A}_2 \Gamma_{\mathbb{I}}(\mathbf{n}_r) \right) [\bar{\mathbf{g}}] = \sum_{r=1}^R c_r \bar{\mathbf{g}} = \bar{\mathbf{g}}, \quad (5.6)$$

and hence equation (5.3) is satisfied. Second we wish to prove that the converse is also true, i.e., if equation (5.3) is satisfied, equation (5.4) is satisfied as well. Let $\mathbb{T}_{\mathbb{A}_2}$ denote a convex combination of the projectors $\Gamma_{\mathbb{A}_2}(\mathbf{n}_r) \mathbb{A}_2$, i.e.,

$$\mathbb{T}_{\mathbb{A}_2} = \left(\sum_{r=1}^R c_r \Gamma_{\mathbb{A}_2}(\mathbf{n}_r) \mathbb{A}_2 \right), \quad (5.7)$$

with

$$c_r > 0 \quad \text{and} \quad \sum_{r=1}^R c_r = 1. \quad (5.8)$$

Then, fixed points of the operator $\mathbb{T}_{\mathbb{A}_2}$ lie in the set [94, Lemma 1.4]

$$\mathcal{E} = \bigcap_{r=1}^R \mathcal{E}_r^{\mathbb{A}}. \quad (5.9)$$

Therefore, any eigenvector of the operator $\mathbb{T}_{\mathbb{A}_2}$ corresponding to the eigenvalue one must lie in the intersection of the subspaces $\mathcal{E}_r^{\mathbb{A}}$, which we denote with \mathcal{E} . In particular, if equation (5.3) is satisfied, the element $\bar{\mathbf{g}}$ lies in \mathcal{E} , i.e.,

$$\mathbb{T}_{\mathbb{A}_2}[\bar{\mathbf{g}}] = \bar{\mathbf{g}}, \quad \implies \quad \bar{\mathbf{g}} \in \mathcal{E} \quad (5.10)$$

and equation (5.4) is satisfied as well.

With the result (5.10) at hand, we observe that a necessary and sufficient condition for the regularity of a rank- R CLM is that the space \mathcal{E} is trivial, i.e.,

$$\mathcal{E} = \{\mathbf{0}\}. \quad (5.11)$$

We refer to equation (5.11) as *non-singularity condition* in the following. In the context of linear elastic and linearly viscous materials, we derived the non-singularity condition (5.11) for the spaces $\mathcal{E}_r^{\mathbb{A}}$, such that

$$\mathcal{E}_r^{\mathbb{A}} \subset \text{Sym}(3), \quad \forall r \in \{1, \dots, R\} \quad \text{or} \quad \mathcal{E}_r^{\mathbb{A}} \subset \text{Sym}_0(3), \quad \forall r \in \{1, \dots, R\}. \quad (5.12)$$

However, the presented proof extends to other problems that can be formulated in the form of equation (5.1), such as thermoelastic or piezoelectricity problems [69, §9]. With the goal of using CLMs as building blocks in a DMN architecture, we are interested in whether there are particular choices of the layering directions \mathbf{n}_r and the rank R of the CLM for which the effective properties of a CLM are always non-singular, i.e., the non-singularity condition (5.11) is satisfied. For incompressible suspensions of rigid fibers, we study this question for CLMs with a rigid core material m_1 and an incompressible coating material m_2 .

A.2 Coated layered materials with incompressible coating and rigid core

For applications involving rigid inclusions in incompressible media, we consider CLMs with an incompressible coating material m_2 and a rigid core material m_1 . Therefore, the spaces $\mathcal{E}_r^{\mathbb{A}} \subset \text{Sym}_0(3)$ have the form

$$\mathcal{E}_r^{\mathbb{A}} = \{\mathbf{B} \in \text{Sym}_0(3) \mid \mathbf{B} \cdot (\mathbf{n}_r \otimes_s \mathbf{a}) = 0, \quad \forall \mathbf{a} \in \mathbb{R}^3\}, \quad (5.13)$$

with the dimensions of the spaces $\mathcal{E}_r^{\mathbb{A}}$ and $\text{Sym}_0(3)$ given by

$$\dim(\mathcal{E}_r^{\mathbb{A}}) = 3, \quad \text{and} \quad \dim(\text{Sym}_0(3)) = 5. \quad (5.14)$$

Because the dimension $\dim(\mathcal{E}_1^{\mathbb{A}} + \mathcal{E}_2^{\mathbb{A}})$ is bounded by the dimension of the space $\text{Sym}_0(3)$, such that

$$\dim(\mathcal{E}_1^{\mathbb{A}} + \mathcal{E}_2^{\mathbb{A}}) \leq 5, \quad (5.15)$$

it follows from the dimension of the intersection of the two spaces $\mathcal{E}_1^{\mathbb{A}}$ and $\mathcal{E}_2^{\mathbb{A}}$

$$\dim(\mathcal{E}_1^{\mathbb{A}} \cap \mathcal{E}_2^{\mathbb{A}}) = \dim(\mathcal{E}_1^{\mathbb{A}}) + \dim(\mathcal{E}_2^{\mathbb{A}}) - \dim(\mathcal{E}_1^{\mathbb{A}} + \mathcal{E}_2^{\mathbb{A}}), \quad (5.16)$$

that

$$\dim(\mathcal{E}_1^{\mathbb{A}} \cap \mathcal{E}_2^{\mathbb{A}}) \geq 3 + 3 - 5 = 1. \quad (5.17)$$

In other words, the intersection of the spaces $\mathcal{E}_1^{\mathbb{A}}$ and $\mathcal{E}_2^{\mathbb{A}}$ is at least one dimensional. Consequently, two layering directions are not sufficient to satisfy the condition (5.11). Besides the required number of layerings, we are also interested in whether there are restrictions on the angles between the layering directions. Suppose that one layering direction is orthogonal to the other two. We discuss the case that the direction \mathbf{n}_3 is orthogonal to the normals \mathbf{n}_1 and \mathbf{n}_2 . The other cases work similarly via permuting the indices. Then it holds that

$$\mathbf{n}_3 \cdot \mathbf{n}_1 = 0, \quad \text{and} \quad \mathbf{n}_3 \cdot \mathbf{n}_2 = 0, \quad (5.18)$$

and the intersection $\mathcal{E}_1^A \cap \mathcal{E}_2^A \cap \mathcal{E}_3^A$ does not only contain the zero element $\mathbf{0}$. Hence, the condition (5.11) is violated. To show this, we consider the alternative description of the spaces \mathcal{E}_r^A

$$\mathcal{E}_r^A = \{\mathbf{B} \in \text{Sym}_0(3) \mid \mathbf{B}\mathbf{n}_r = \alpha\mathbf{n}_r \text{ for some } \alpha \in \mathbb{R}\} \quad (5.19)$$

which is equivalent to equation (5.13) and characterizes the space \mathcal{E}_r^A via all tensors $\mathbf{B} \in \mathcal{E}_r^A$ that have the layering direction \mathbf{n}_r as an eigenvector. Then the tensor

$$\mathbf{B} = \mathbf{n}_1 \otimes \mathbf{n}_1 + \mathbf{m}_2 \otimes \mathbf{m}_2 - 2\mathbf{n}_3 \otimes \mathbf{n}_3, \quad (5.20)$$

where the layering direction \mathbf{m}_2 is constructed by orthogonalization, such that

$$\mathbf{m}_2 = \mathbf{n}_2 - (\mathbf{n}_1 \cdot \mathbf{n}_2)\mathbf{n}_1, \quad (5.21)$$

is an element of the intersection $\mathcal{E}_1^A \cap \mathcal{E}_2^A \cap \mathcal{E}_3^A$. This is true because it holds that

$$\text{tr}(\mathbf{B}) = 0, \quad \mathbf{B}\mathbf{n}_1 = \mathbf{n}_1, \quad \mathbf{B}\mathbf{n}_2 = \mathbf{n}_2, \quad \mathbf{B}\mathbf{n}_3 = \mathbf{n}_3, \quad (5.22)$$

and therefore condition (5.11) is violated. In other words, the effective properties $\bar{\mathbb{A}}$ of a rank-3 CLM with incompressible coating and rigid core, where one layering direction \mathbf{n}_3 is orthogonal to the other two layering directions \mathbf{n}_1 and \mathbf{n}_2 , is always singular. Particularly, if all three layering directions are mutually orthogonal, the effective properties $\bar{\mathbb{A}}$ of a rank-3 CLM are singular.

In contrast, let the three layering directions be mutually non-orthogonal and mutually non-collinear, i.e.,

$$0 < |\mathbf{n}_1 \cdot \mathbf{n}_2| < 1, \quad 0 < |\mathbf{n}_1 \cdot \mathbf{n}_3| < 1, \quad 0 < |\mathbf{n}_2 \cdot \mathbf{n}_3| < 1. \quad (5.23)$$

We consider an element \mathbf{B} in the intersection $\mathcal{E}_1^A \cap \mathcal{E}_2^A \cap \mathcal{E}_3^A$ and wish to show that the tensor \mathbf{B} vanishes, such that the non-singularity condition (5.11) is satisfied. Because the tensor \mathbf{B} is symmetric, its eigenvectors corresponding to distinct eigenvalues are orthogonal. Thus, if the eigenvalues were distinct, the layering directions would need to be orthogonal. However, this contradicts our assumption (5.23). Therefore, the tensor \mathbf{B} has a single eigenvalue α with the corresponding eigenspace \mathbb{R}^3 , i.e., the tensor \mathbf{B} attains the form

$$\mathbf{B} = \alpha\mathbf{I}, \quad \alpha \in \mathbb{R}. \quad (5.24)$$

Additionally, because the trace of the tensor \mathbf{B} vanishes, i.e., $\text{tr}(\mathbf{B}) = 0$, it follows that the eigenvalue α is zero. Consequently, the tensor \mathbf{B} must vanish, the non-singularity condition (5.11) is satisfied, and the effective properties $\bar{\mathbb{A}}$ of a rank-3 CLM with an incompressible coating material m_2 and a rigid core material m_1 are non-singular, if the three layering directions are mutually non-orthogonal and non-collinear.

References

- [1] Y. Swolfs, "Perspective for fibre-hybrid composites in wind energy applications," *Materials*, vol. 10, no. 11, p. 1281, 2017.
- [2] A. Wazeer, A. Das, C. Abeykoon, A. Sinha, and A. Karmakar, "Composites for electric vehicles and automotive sector: A review," *Green Energy and Intelligent Transportation*, vol. 2, no. 1, p. 100043, 2023.
- [3] D. M. Botín-Sanabria, A.-S. Mihaitea, R. E. Peimbert-García, M. A. Ramírez-Moreno, R. A. Ramírez-Mendoza, and J. d. J. Lozoya-Santos, "Digital twin technology challenges and applications: A comprehensive review," *Remote Sensing*, vol. 14, no. 6, p. 1335, 2022.
- [4] F. Henning, L. Kärger, D. Dörr, F. J. Schirmaier, J. Seuffert, and A. Bernath, "Fast processing and continuous simulation of automotive structural composite components," *Composites Science and Technology*, vol. 171, pp. 261–279, 2019.

- [5] J. Görthofer, N. Meyer, T. D. Pallicity, L. Schöttl, A. Trauth, M. Schemmann, M. Hohberg, P. Pinter, P. Elsner, F. Henning, A. Hrymak, T. Seelig, K. Weidenmann, L. Kärger, and T. Böhlke, “Virtual process chain of sheet molding compound: Development, validation and perspectives,” *Composites Part B: Engineering*, vol. 169, pp. 133–147, 2019.
- [6] N. Meyer, S. Gajek, J. Görthofer, A. Hrymak, L. Kärger, F. Henning, M. Schneider, and T. Böhlke, “A probabilistic virtual process chain to quantify process-induced uncertainties in sheet molding compounds,” *Composites Part B: Engineering*, vol. 249, p. 110380, 2023.
- [7] J. Castro and G. Tomlinson, “Predicting molding forces in SMC compression molding,” *Polymer Engineering & Science*, vol. 30, no. 24, pp. 1568–1573, 1990.
- [8] V. Goodship, *ARBURG practical guide to injection moulding*. Shawbury, United Kingdom: Smithers Rapra, 2017.
- [9] H.-C. Tseng, R.-Y. Chang, and C.-H. Hsu, “Predictions of fiber concentration in injection molding simulation of fiber-reinforced composites,” *Journal of Thermoplastic Composite Materials*, vol. 31, no. 11, pp. 1529–1544, 2018.
- [10] T. Karl, D. Gatti, T. Böhlke, and B. Frohnapfel, “Coupled simulation of flow-induced viscous and elastic anisotropy of short-fiber reinforced composites,” *Acta Mechanica*, vol. 232, no. 6, pp. 2249–2268, 2021.
- [11] S. Mortazavian and A. Fatemi, “Effects of fiber orientation and anisotropy on tensile strength and elastic modulus of short fiber reinforced polymer composites,” *Composites part B: engineering*, vol. 72, pp. 116–129, 2015.
- [12] T. Böhlke, F. Henning, A. N. Hrymak, L. Kärger, K. Weidenmann, and J. T. Wood, *Continuous–Discontinuous Fiber-Reinforced Polymers: An Integrated Engineering Approach*. Carl Hanser Verlag GmbH Co KG, 2019.
- [13] T. Karl and T. Böhlke, “Unified mean-field modeling of viscous short-fiber suspensions and solid short-fiber reinforced composites,” *Archive of Applied Mechanics*, vol. 92, no. 12, pp. 3695–3727, 2022.
- [14] M. Sepehr, P. J. Carreau, M. Moan, and G. Ausias, “Rheological properties of short fiber model suspensions,” *Journal of Rheology*, vol. 48, no. 5, pp. 1023–1048, 2004.
- [15] S. M. Dinh and R. C. Armstrong, “A rheological equation of state for semiconcentrated fiber suspensions,” *Journal of Rheology*, vol. 28, no. 3, pp. 207–227, 1984.
- [16] M. M. Cross, “Rheology of Non-Newtonian fluids: a new flow equation for pseudoplastic systems,” *Journal of Colloid Science*, vol. 20, no. 5, pp. 417–437, 1965.
- [17] B. Sterr, D. Wicht, A. Hrymak, M. Schneider, and T. Böhlke, “Homogenizing the viscosity of shear-thinning fiber suspensions with an FFT-based computational method,” *Journal of Non-Newtonian Fluid Mechanics*, vol. 321, p. 105101, 2023.
- [18] M. L. Williams, R. F. Landel, and J. D. Ferry, “The temperature dependence of relaxation mechanisms in amorphous polymers and other glass-forming liquids,” *Journal of the American Chemical society*, vol. 77, no. 14, pp. 3701–3707, 1955.
- [19] R. B. Pipes, J. Hearle, A. Beaussart, A. Sastry, and R. Okine, “A constitutive relation for the viscous flow of an oriented fiber assembly,” *Journal of Composite Materials*, vol. 25, no. 9, pp. 1204–1217, 1991.
- [20] J. D. Goddard, “Tensile stress contribution of flow-oriented slender particles in Non-Newtonian fluids,” *Journal of Non-Newtonian Fluid Mechanics*, vol. 1, no. 1, pp. 1–17, 1976.
- [21] J. Goddard, “The stress field of slender particles oriented by a Non-Newtonian extensional flow,” *Journal of Fluid Mechanics*, vol. 78, no. 1, pp. 177–206, 1976.
- [22] B. Souloumiac and M. Vincent, “Steady shear viscosity of short fibre suspensions in thermoplastics,” *Rheologica Acta*, vol. 37, no. 3, pp. 289–298, 1998.
- [23] C. Mobuchon, P. J. Carreau, M.-C. Heuzey, M. Sepehr, and G. Ausias, “Shear and extensional properties of short glass fiber reinforced polypropylene,” *Polymer Composites*, vol. 26, no. 3, pp. 247–264, 2005.
- [24] J. Férec, E. Bertevas, B. C. Khoo, G. Ausias, and N. Phan-Thien, “The effect of shear-thinning behaviour on rod orientation in filled fluids,” *Journal of Fluid Mechanics*, vol. 798, pp. 350–370, 2016.
- [25] J. Ericksen, “Transversely isotropic fluids,” *Colloid and Polymer Science*, vol. 173, pp. 117–122, 1960.
- [26] C. L. Tucker III, “Flow regimes for fiber suspensions in narrow gaps,” *Journal of Non-Newtonian fluid mechanics*, vol. 39, no. 3, pp. 239–268, 1991.
- [27] R. B. Pipes, “Anisotropic viscosities of an oriented fiber composite with a power-law matrix,” *Journal of Composite Materials*, vol. 26, no. 10, pp. 1536–1552, 1992.
- [28] D. Coffin and R. B. Pipes, “Constitutive relationships for aligned discontinuous fibre composites,” *Composites Manufacturing*, vol. 2, no. 3-4, pp. 141–146, 1991.

- [29] R. B. Pipes, D. W. Coffin, S. F. Shuler, and P. Šimáček, “Non-Newtonian constitutive relationships for hyperconcentrated fiber suspensions,” *Journal of Composite Materials*, vol. 28, no. 4, pp. 343–351, 1994.
- [30] D. Binding, “Capillary and contraction flow of long-(glass) fibre filled polypropylene,” *Composites Manufacturing*, vol. 2, no. 3-4, pp. 243–252, 1991.
- [31] A. J. Favaloro, H.-C. Tseng, and R. B. Pipes, “A new anisotropic viscous constitutive model for composites molding simulation,” *Composites Part A: Applied Science and Manufacturing*, vol. 115, pp. 112–122, 2018.
- [32] H.-C. Tseng, “A constitutive equation for fiber suspensions in viscoelastic media,” *Physics of Fluids*, vol. 33, no. 7, p. 071702, 2021.
- [33] M. Khan, R. V. More, and A. M. Ardekani, “A constitutive model for sheared dense fiber suspensions,” *Physics of Fluids*, vol. 35, no. 1, 2023.
- [34] C. Schelleis, A. Hrymak, and F. Henning, “Optimizing processing parameters for glass fiber reinforced polycarbonate lft-d composites,” *Society for the Advancement of Material and Process Engineering Europe Conference*, 2023.
- [35] A. R. Eschbach, “Dynamic shear rheometer and method,” Dec. 21 1993. US Patent 5,271,266.
- [36] O. Švec, J. Skoček, H. Stang, M. R. Geiker, and N. Roussel, “Free surface flow of a suspension of rigid particles in a non-Newtonian fluid: A lattice Boltzmann approach,” *Journal of Non-Newtonian Fluid Mechanics*, vol. 179, pp. 32–42, 2012.
- [37] J. Domurath, G. Ausias, J. Férec, and M. Saphiannikova, “Numerical investigation of dilute suspensions of rigid rods in power-law fluids,” *Journal of Non-Newtonian Fluid Mechanics*, vol. 280, p. 104280, 2020.
- [38] R. Bertóti, D. Wicht, A. Hrymak, M. Schneider, and T. Böhlke, “A computational investigation of the effective viscosity of short-fiber reinforced thermoplastics by an FFT-based method,” *European Journal of Mechanics-B/Fluids*, vol. 90, pp. 99–113, 2021.
- [39] M. Schneider, “A review of nonlinear FFT-based computational homogenization methods,” *Acta Mechanica*, vol. 232, no. 6, pp. 2051–2100, 2021.
- [40] T. Kanit, S. Forest, I. Galliet, V. Mounoury, and D. Jeulin, “Determination of the size of the representative volume element for random composites: statistical and numerical approach,” *International Journal of Solids and Structures*, vol. 40, no. 13-14, pp. 3647–3679, 2003.
- [41] J. Renard and M. Marmonier, “Etude de l’initiation de l’endommagement dans la matrice d’un matériau composite par une méthode d’homogénéisation,” *La Recherche aérospatiale*, no. 6, pp. 43–51, 1987.
- [42] F. Feyel, “A multilevel finite element method (fe2) to describe the response of highly non-linear structures using generalized continua,” *Computer Methods in Applied Mechanics and Engineering*, vol. 192, no. 28-30, pp. 3233–3244, 2003.
- [43] J. Spahn, H. Andrä, M. Kabel, and R. Müller, “A multiscale approach for modeling progressive damage of composite materials using fast Fourier transforms,” *Computer Methods in Applied Mechanics and Engineering*, vol. 268, pp. 871–883, 2014.
- [44] J. Kochmann, S. Wulfinghoff, S. Reese, J. R. Mianroodi, and B. Svendsen, “Two-scale FE-FFT-and phase-field-based computational modeling of bulk microstructural evolution and macroscopic material behavior,” *Computer Methods in Applied Mechanics and Engineering*, vol. 305, pp. 89–110, 2016.
- [45] J. Kochmann, L. Ehle, S. Wulfinghoff, J. Mayer, B. Svendsen, and S. Reese, “Efficient multiscale FE-FFT-based modeling and simulation of macroscopic deformation processes with non-linear heterogeneous microstructures,” *Multiscale Modeling of Heterogeneous Structures*, pp. 129–146, 2018.
- [46] S. Gajek, M. Schneider, and T. Böhlke, “An FE-DMN method for the multiscale analysis of short fiber reinforced plastic components,” *Computer Methods in Applied Mechanics and Engineering*, vol. 384, p. 113952, 2021.
- [47] N. R. Ashwin, Z. Cao, N. Muralidhar, D. Tafti, and A. Karpatne, “Deep learning methods for predicting fluid forces in dense particle suspensions,” *Powder Technology*, vol. 401, p. 117303, 2022.
- [48] N. R. Ashwin, D. Tafti, N. Muralidhar, and Z. Cao, “Physics informed deep learning for flow and force predictions in dense ellipsoidal particle suspensions,” *Powder Technology*, p. 119684, 2024.
- [49] O. Ronneberger, P. Fischer, and T. Brox, “U-net: Convolutional networks for biomedical image segmentation,” in *Medical image computing and computer-assisted intervention—MICCAI 2015: 18th international conference, Munich, Germany, October 5–9, 2015, proceedings, part III 18*, pp. 234–241, Springer, 2015.
- [50] M. Boodaghidizaji, M. Khan, and A. M. Ardekani, “Multi-fidelity modeling to predict the rheological properties of a suspension of fibers using neural networks and Gaussian processes,” *Physics of Fluids*, vol. 34, no. 5, 2022.

- [51] Sterr, Benedikt and Hrymak, Andrew and Schneider, Matti and Böhlke, Thomas, “Machine learning assisted discovery of effective viscous material laws for shear-thinning fiber suspensions,” Computational Mechanics, pp. 1–19, 2024.
- [52] Z. Liu, C. Wu, and M. Koishi, “A deep material network for multiscale topology learning and accelerated nonlinear modeling of heterogeneous materials,” Computer Methods in Applied Mechanics and Engineering, vol. 345, pp. 1138–1168, 2019.
- [53] Z. Liu and C. Wu, “Exploring the 3D architectures of deep material network in data-driven multiscale mechanics,” Journal of the Mechanics and Physics of Solids, vol. 127, pp. 20–46, 2019.
- [54] S. Gajek, M. Schneider, and T. Böhlke, “On the micromechanics of deep material networks,” Journal of the Mechanics and Physics of Solids, vol. 142, p. 103984, 2020.
- [55] J. Köbler, M. Schneider, F. Ospald, H. Andrä, and R. Müller, “Fiber orientation interpolation for the multiscale analysis of short fiber reinforced composite parts,” Computational Mechanics, vol. 61, pp. 729–750, 2018.
- [56] Z. Liu, C. Wu, and M. Koishi, “Transfer learning of deep material network for seamless structure–property predictions,” Computational Mechanics, vol. 64, no. 2, pp. 451–465, 2019.
- [57] T. Huang, Z. Liu, C. Wu, and W. Chen, “Microstructure-guided deep material network for rapid nonlinear material modeling and uncertainty quantification,” Computer Methods in Applied Mechanics and Engineering, vol. 398, p. 115197, 2022.
- [58] T. Li, “Micromechanics-informed parametric deep material network for physics behavior prediction of heterogeneous materials with a varying morphology,” Computer Methods in Applied Mechanics and Engineering, vol. 419, p. 116687, 2024.
- [59] S. Gajek, M. Schneider, and T. Böhlke, “An FE-DMN method for the multiscale analysis of thermomechanical composites,” Computational Mechanics, vol. 69, no. 5, pp. 1087–1113, 2022.
- [60] D. Shin, R. Alberdi, R. A. Lebensohn, and R. Dingreville, “A deep material network approach for predicting the thermomechanical response of composites,” Composites Part B: Engineering, vol. 272, p. 111177, 2024.
- [61] A. P. Dey, F. Welschinger, M. Schneider, S. Gajek, and T. Böhlke, “Training deep material networks to reproduce creep loading of short fiber-reinforced thermoplastics with an inelastically-informed strategy,” Archive of Applied Mechanics, vol. 92, no. 9, pp. 2733–2755, 2022.
- [62] A. P. Dey, F. Welschinger, M. Schneider, S. Gajek, and T. Böhlke, “Rapid inverse calibration of a multiscale model for the viscoplastic and creep behavior of short fiber-reinforced thermoplastics based on Deep Material Networks,” International Journal of Plasticity, vol. 160, p. 103484, 2023.
- [63] A. P. Dey, F. Welschinger, M. Schneider, J. Köbler, and T. Böhlke, “On the effectiveness of deep material networks for the multi-scale virtual characterization of short fiber-reinforced thermoplastics under highly nonlinear load cases,” Archive of Applied Mechanics, pp. 1–26, 2024.
- [64] Z. Liu, “Deep material network with cohesive layers: Multi-stage training and interfacial failure analysis,” Computer Methods in Applied Mechanics and Engineering, vol. 363, p. 112913, 2020.
- [65] Z. Liu, “Cell division in deep material networks applied to multiscale strain localization modeling,” Computer Methods in Applied Mechanics and Engineering, vol. 384, p. 113914, 2021.
- [66] L. Wu, L. Adam, and L. Noels, “Micro-mechanics and data-driven based reduced order models for multi-scale analyses of woven composites,” Composite Structures, vol. 270, p. 114058, 2021.
- [67] V. D. Nguyen and L. Noels, “Interaction-based material network: A general framework for (porous) microstructured materials,” Computer Methods in Applied Mechanics and Engineering, vol. 389, p. 114300, 2022.
- [68] V. D. Nguyen and L. Noels, “Micromechanics-based material networks revisited from the interaction viewpoint; robust and efficient implementation for multi-phase composites,” European Journal of Mechanics-A/Solids, vol. 91, p. 104384, 2022.
- [69] G. W. Milton, The Theory of Composites. SIAM, 2002.
- [70] M. Kabel, F. Ospald, and M. Schneider, “A model order reduction method for computational homogenization at finite strains on regular grids using hyperelastic laminates to approximate interfaces,” Computer Methods in Applied Mechanics and Engineering, vol. 309, pp. 476–496, 2016.
- [71] D. G. Edelen, “On the existence of symmetry relations and dissipation potentials,” Archive for Rational Mechanics and Analysis, vol. 51, pp. 218–227, 1973.
- [72] R. Hill, “Elastic properties of reinforced solids: some theoretical principles,” Journal of the Mechanics and Physics of Solids, vol. 11, no. 5, pp. 357–372, 1963.

- [73] J. Mandel, "Contribution théorique à l'étude de l'érouissage et des lois de l'écoulement plastique," in Applied Mechanics: Proceedings of the Eleventh International Congress of Applied Mechanics Munich (Germany) 1964, pp. 502–509, Springer, 1966.
- [74] A. B. Owen, "Scrambling Sobol' and Niederreiter–Xing Points," Journal of Complexity, vol. 14, no. 4, pp. 466–489, 1998.
- [75] I. Sobol', "On the distribution of points in a cube and the approximate evaluation of integrals," USSR Computational Mathematics and Mathematical Physics, vol. 7, no. 4, pp. 86–112, 1967.
- [76] A. Paszke, S. Gross, F. Massa, A. Lerer, J. Bradbury, G. Chanan, T. Killeen, Z. Lin, N. Gimeshein, L. Antiga, A. Desmaison, A. Kopf, E. Yang, Z. DeVito, M. Raison, A. Tejani, S. Chilamkurthy, B. Steiner, L. Fang, J. Bai, and S. Chintala, "PyTorch: An Imperative Style, High-Performance Deep Learning Library," in Advances in Neural Information Processing Systems 32, pp. 8024–8035, Curran Associates, Inc., 2019.
- [77] L. Liu, H. Jiang, P. He, W. Chen, X. Liu, J. Gao, and J. Han, "On the variance of the adaptive learning rate and beyond," arXiv preprint arXiv:1908.03265, 2019.
- [78] A. Neumaier, "Solving ill-conditioned and singular linear systems: A tutorial on regularization," SIAM Review, vol. 40, no. 3, pp. 636–666, 1998.
- [79] P. Kennedy and R. Zheng, Flow Analysis of Injection Molds. Munich, Germany: Carl Hanser Verlag GmbH Co KG, 2013.
- [80] M.-L. Wang, R.-Y. Chang, and C.-H. D. Hsu, Molding simulation: Theory and practice. Carl Hanser Verlag GmbH Co KG, 2018.
- [81] K. Kanatani, "Distribution of directional data and fabric tensors," International Journal of Engineering Science, vol. 22, no. 2, pp. 149–164, 1984.
- [82] S. G. Advani and C. L. Tucker III, "The use of tensors to describe and predict fiber orientation in short fiber composites," Journal of Rheology, vol. 31, no. 8, pp. 751–784, 1987.
- [83] J. S. Cintra Jr and C. L. Tucker III, "Orthotropic closure approximations for flow-induced fiber orientation," Journal of Rheology, vol. 39, no. 6, pp. 1095–1122, 1995.
- [84] J. K. Bauer and T. Böhlke, "Variety of fiber orientation tensors," Mathematics and Mechanics of Solids, vol. 27, no. 7, pp. 1185–1211, 2022.
- [85] J. K. Bauer, M. Schneider, and T. Böhlke, "On the phase space of fourth-order fiber-orientation tensors," Journal of Elasticity, vol. 153, no. 2, pp. 161–184, 2023.
- [86] M. Schneider, "The sequential addition and migration method to generate representative volume elements for the homogenization of short fiber reinforced plastics," Computational Mechanics, vol. 59, no. 2, pp. 247–263, 2017.
- [87] "Ultramid®B3K Polyamide 6 Material data." <https://www.campusplastics.com/campus/de/datasheet/Ultramid%C2%AE+B3K/BASF/20/3a22f000>. Accessed: 2020-09-26.
- [88] F. H. Harlow and J. E. Welch, "Numerical calculation of time-dependent viscous incompressible flow of fluid with free surface," The Physics of Fluids, vol. 8, no. 12, pp. 2182–2189, 1965.
- [89] L. N. Smith and N. Topin, "Super-convergence: Very fast training of neural networks using large learning rates," in Artificial Intelligence and Machine Learning for Multi-Domain Operations Applications, vol. 11006, pp. 369–386, SPIE, 2019.
- [90] C. Darken and J. Moody, "Note on learning rate schedules for stochastic optimization," Advances in Neural Information Processing Systems, vol. 3, 1990.
- [91] C. Darken, J. Chang, and J. Moody, "Learning rate schedules for faster stochastic gradient search," in Neural Networks For Signal Processing, vol. 2, pp. 3–12, Citeseer, 1992.
- [92] S. F. Shuler, D. M. Binding, and R. Byron Pipes, "Rheological behavior of two- and three-phase fiber suspensions," Polymer Composites, vol. 15, no. 6, pp. 427–435, 1994.
- [93] H. Cui and J. R. Grace, "Flow of pulp fibre suspension and slurries: A review," International Journal of Multiphase Flow, vol. 33, no. 9, pp. 921–934, 2007.
- [94] S. Reich, "A limit theorem for projections," Linear and Multilinear Algebra, vol. 13, no. 3, pp. 281–290, 1983.